ANNUAL
REVIEWS

Annual Review of Fluid Mechanics

Capillary Drainage in Horizontal Soap Films: Theoretical Review and Experimental Illustrations

Isabelle Cantat,[1,2] Savinien Pertant,[1]
Christophe Raufaste,[2,3] and Emmanuelle Rio[4]

[1] Université de Rennes, CNRS, IPR (Institut de Physique de Rennes) - UMR 6251, Rennes, France; email: isabelle.cantat@univ-rennes.fr

[2] Institut Universitaire de France, Paris, France

[3] Université Côte d'Azur, CNRS, INPHYNI, Nice, France

[4] Université Paris-Saclay, CNRS, Laboratoire de Physique des Solides, Orsay, France

Annu. Rev. Fluid Mech. 2026. 58:111–38

The *Annual Review of Fluid Mechanics* is online at fluid.annualreviews.org

https://doi.org/10.1146/annurev-fluid-100224-111138

Keywords

free surface flow, thin film, surfactant, foam, Marangoni flows, drainage, lubrication, marginal regeneration, Gibbs elasticity, thin film balance

Abstract

Soap films and bubbles are inherently unstable systems that evolve over time. Their thickness is primarily governed by the competition between capillary and viscous forces. The presence of surfactants introduces Marangoni stresses, which limit interfacial extension and significantly increase film lifetime. While the bulk flow is typically well-described by a simple Poiseuille profile between the two interfaces, the interfacial dynamics can induce complex behaviors, even in the simple case of horizontal film drainage, which is used as a paradigmatic example in this review. The interfacial velocity is dictated by the thickness gradients and by the interfacial rheology, which, in many practical cases, reduces to the condition of an incompressible interface. This simplified framework allows for analytical predictions and scaling laws in axisymmetric flows. It is also consistent with the spontaneous symmetry breaking that may be observed in horizontal films—a phenomenon associated with the marginal regeneration process, which remains only partially understood. This review presents the most elementary theoretical frameworks capable of capturing the essential features of these flows and provides quantitative comparisons with available experimental data.

1. INTRODUCTION

Disjoining pressure: pressure term in thin films due to short-range forces

Marginal regeneration: instability occurring between a thin film and a meniscus; it leads to the extraction, from the meniscus, of patches of film thinner than the surrounding film

The thinning dynamics of a liquid film trapped between two bubbles, known as film drainage, is an active research topic with major industrial challenges, involving chemistry, hydrodynamics, and nonequilibrium thermodynamics. The trapped film is nearly flat, while the liquid surrounding the film, generally referred to as the meniscus, is at a lower Laplace pressure than the film itself. As a result, the film drains until it stabilizes due to the disjoining pressure, it ruptures, or the bubbles separate.

In a bubbly liquid, this thinning process determines the likelihood of coalescence before the bubbles drift apart, thereby influencing bubble size distribution in many industrial processes (Kamp et al. 2017). The same governing principles apply when a bubble reaches the surface of a liquid bath. In this case, the film thickness at the moment of rupture dictates the size distribution of ejected droplets—an important factor in various fields, including aerosol production at the ocean surface (Bird et al. 2010, Modini et al. 2013, Deike 2022, Jiang et al. 2024). In liquid foams, films are continuously renewed by bubble rearrangements, known as T1 events, where two bubbles come into contact and form a new film. If the relaxation time for the film thickness to reach equilibrium is shorter than the interval between two successive T1 events on the same bubble, the film thickness reaches equilibrium, governed by disjoining pressure. Otherwise, the average film thickness in a foam is controlled by its film drainage time, hence modifying the foam coarsening rate (Saint-Jalmes & Trégouët 2023).

To distinguish this work from recent reviews on the subject (Chan et al. 2011, Chatzigiannakis et al. 2021), we mainly focus on the purely hydrodynamic aspects of the problem, involving films thicker than 100 nm with negligible disjoining pressure. We adopt a primarily theoretical perspective in an attempt to identify the minimal ingredients responsible for the observed flows. A central example discussed in this review is the capillary drainage of a horizontal film. As illustrated in **Figure 1*a–c***, this seemingly simple situation can involve symmetry breaking, giving rise to complex flow patterns. The surprisingly regular structures observed near the menisci were first investigated by Mysels et al. (1959) under the name of marginal regeneration and have recently attracted renewed interest.

Liquid films are characterized by a thickness much smaller than the other relevant dimensions, justifying geometric simplifications. If we define the dry skeleton of a film as the geometric surface equidistant from its two interfaces, we obtain a simplified structure that, at equilibrium, is governed by the laws established by Plateau (1873). The fluid mechanics of soap films predicts the motion occurring tangential to the dry skeleton and lies between a 2D and 3D problem. In a 2D framework, the film element, shown in **Figure 2**, serves a role analogous to that of an elementary fluid particle in a 3D flow. These elementary volumes, spanning from one interface to the other, are characterized by their thickness $2h$ and surface area $\mathrm{d}A$, defined as the intersection of the film element with its dry skeleton. Given the film's small thickness, $\mathrm{d}A$ almost equals the area of the top or bottom interface elements $\mathrm{d}A_\mathrm{t}$ and $\mathrm{d}A_\mathrm{b}$, respectively.

Film elements are particularly useful for analyzing flows in which both interfaces move at the same velocity. In such cases, $\mathrm{d}A_\mathrm{t}$ and $\mathrm{d}A_\mathrm{b}$ undergo identical deformations and trajectories, remaining in front of each other. In this review, we focus on these symmetric situations (which include bubbles with a curved skeleton), and the film element is thus the volume of fluid between the two interfaces $\mathrm{d}A_\mathrm{t}$ and $\mathrm{d}A_\mathrm{b}$, tracked along their trajectories. Since the bulk fluid does not necessarily flow at the same velocity as the interfaces, a film element represents an open system: It can gain or lose mass, deform by shear or extensional deformation, and move as a whole within the plane of the film.

After establishing a theoretical framework for describing these flows in Section 2, we use in Section 3 the example of film extraction to discuss the limit of interfaces that strongly resist

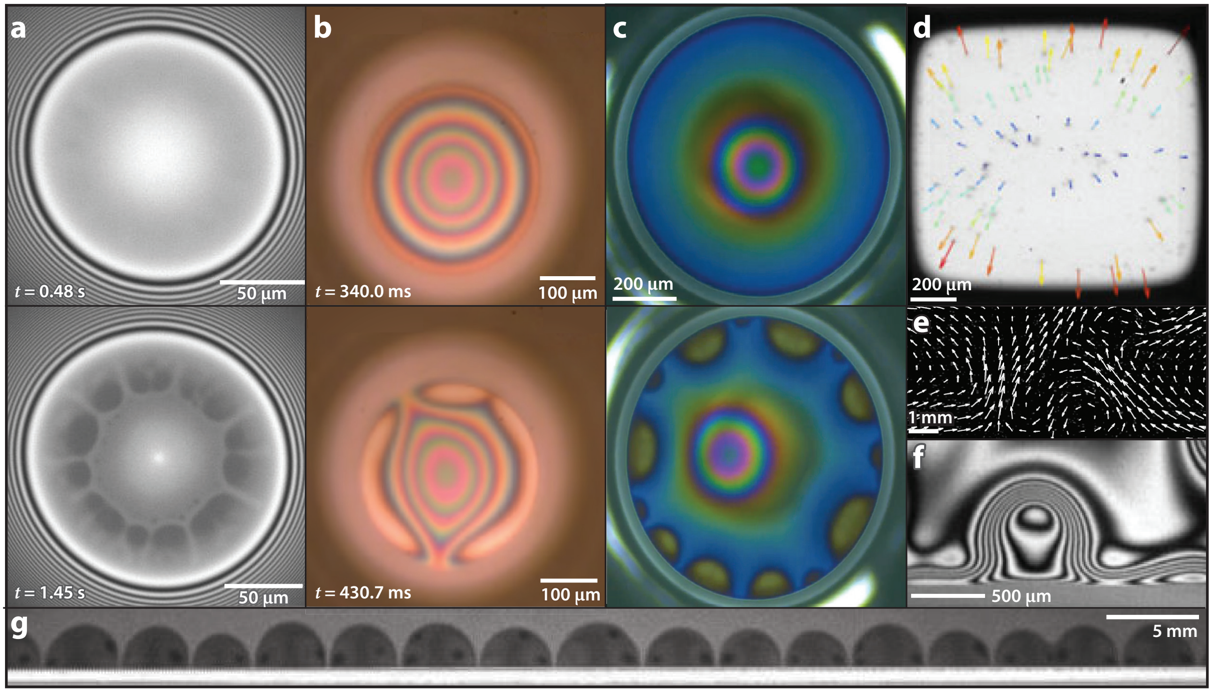

Figure 1

Film thickness field observed by (*a–c*, *f*) interference or (*g*) fluorescence during capillary drainage. At short times, a dimple forms, the film being the thickest at the center and separated from the surrounding meniscus by a thinner groove (also denoted as a barrier rim or pinch). This groove may destabilize, forming semicircular patches of thin film along the meniscus. Panels *f* and *g* show close-up views in the vicinity of a meniscus. The velocity fields indicate (*d*) axisymmetric extension or (*e*) more complex flows. Films are horizontal except in panels *e* and *f*. Panel *a* adapted from Mikhailovskaya et al. (2022) (CC BY 4.0). Panel *b* adapted with permission from Liu et al. (2018). Panel *c* adapted from Frostad et al. (2016). Panel *d* adapted from Petit et al. (2015). Panels *e* and *f* adapted with permission from Lhuissier & Villermaux (2012). Panel *g* adapted from photo provided by Sanjiban Nath.

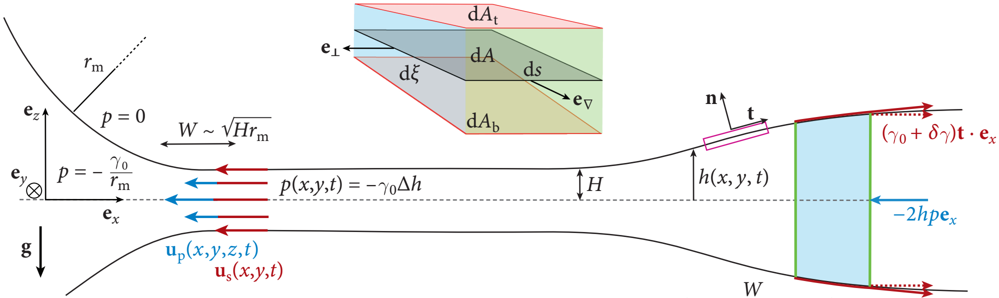

Figure 2

Generic film geometry and notations used in the article. The film is in contact with a meniscus on the left and exhibits thickness variations on the right. A 3D view of a film element is shown, with the same color-coding as in the main 2D representation. The unit vector $\mathbf{e}_\nabla$ is oriented along the thickness gradient [$\mathbf{e}_\nabla = \mathbf{e}_x$ in the example but it may be oriented in any direction in the (x, y) plane]. The magenta box at the top interface is used to express the tangential stress continuity discussed in Section 2.2.

Table 1 Regime of validity of the equations discussed in the review, characterized by $\varepsilon = H/W$

Number name	Notation	Order of magnitude
Film thickness	H	≥ 100 nm
Reynolds number	$Re_{\mathrm{P}} = \dfrac{\rho W U_{\mathrm{P}}}{\eta}$	$\leq \varepsilon$
Bond number	$Bo = \dfrac{\rho g H^2}{\gamma_0}$	$\leq \varepsilon^3$
Velocity ratio	$\dfrac{U_{\mathrm{S}}}{U_{\mathrm{P}}}$	$\leq 1/\varepsilon$
Capillary number	$Ca_{\mathrm{P}} = \dfrac{\eta U_{\mathrm{P}}}{\gamma_0}$	ε^3
Boussinesq number time velocity ratio	$Bq\dfrac{U_{\mathrm{S}}}{U_{\mathrm{P}}} = \dfrac{\eta_{\mathrm{s}}}{\eta H}\dfrac{U_{\mathrm{S}}}{U_{\mathrm{P}}}$	$1/\varepsilon^2$ (if[a])
Tension variation	$\dfrac{\delta\gamma}{\gamma_0}$	ε^2 (if[b])

In the model derivation, assumptions are made a priori on H, Re_{P}, Bo, and $U_{\mathrm{S}}/U_{\mathrm{P}}$ to establish the equations of motion. The solution of these equations then imposes conditions for Ca_{P}, $Bq(U_{\mathrm{S}}/U_{\mathrm{P}})$, and $\delta\gamma$ with the following restrictions.

[a] For generic flows, without axisymmetry or invariance under translation, otherwise U_{S} may be equal to zero.

[b] If the experimental timescale satisfies $\tau^{\mathrm{exp}} \ll (\eta_{\mathrm{s}} + \kappa_{\mathrm{s}})/E$.

extension and thus reach the incompressible interface limit. Section 4 then focuses on axisymmetric drainage, discussing recent observations in light of classical analytical results, while Section 5 addresses the intriguing question of the origin of symmetry breaking.

2. EQUATION OF MOTION IN THE LUBRICATION REGIME

A typical soap film is schematized in **Figure 2**. The scale in the z direction is highly exaggerated, and two distinct length scales can be defined: the film thickness scale H and the characteristic length W over which the thickness varies. Near the film–meniscus boundary, W is set by the meniscus radius of curvature r_{m}. Indeed, in this domain, the curvature scales both as H/W^2 and $1/r_{\mathrm{m}}$, giving $W = \sqrt{H r_{\mathrm{m}}}$. In other cases, W depends on the film's initial shape, but the ratio $\varepsilon = H/W$ is still much smaller than one.

The equations of motion are derived by performing a Taylor expansion of the Navier–Stokes equations and of their boundary conditions, using ε as a small parameter. Systematic expansions, as described by Oron et al. (1997) and Breward (1999) for a single in-plane variable (e.g., the variable x in **Figure 2**) or by Chomaz (2001) and Shi et al. (2022) for the general case, require choosing a priori the orders of magnitude for the dimensionless numbers involved. Capillary drainage, in the presence of surfactant, is usually ruled by the constraints gathered in **Table 1**, which are progressively discussed throughout Section 2. Soap films can accommodate a wide range of parameters under these constraints, with typical values provided in **Table 2**. Unless otherwise specified, the orders of magnitude are estimated with these values.

In-plane flows are decoupled from the film's dry skeleton shape (under the conditions given in Section 2.1), so we can assume it is planar. As shown in **Figure 2**, we study a horizontal film of thickness $2h(x, y, t)$, symmetric with respect to the (x, y) plane. The Laplacian Δ and gradient ∇ refer to 2D operators in this plane.

The velocity field is characterized by two independent velocity scales: U_{S} for the interface velocity $\mathbf{u}_{\mathrm{s}}(x, y) = \mathbf{u}(x, y, \pm h)$ and U_{P} for the bulk velocity relative to the interfaces, defined as $\mathbf{u}_{\mathrm{p}}(x, y, z) = \mathbf{u}(x, y, z) - \mathbf{u}_{\mathrm{s}}(x, y)$ (see **Figure 2**). The latter follows a parabolic Poiseuille profile, justifying its notation.

Table 2 Orders of magnitude representative of the flow regime defined in Table 1 and of most of the discussed examples

Quantity	Notation	Representative value
Film thickness	H	10^{-6} m
Meniscus radius of curvature	r_m	10^{-4} m
Horizontal length scale[a]	W	10^{-5} m
Surface tension[b]	γ_0	3×10^{-2} kg/s^2
Bulk viscosity[b]	η	10^{-3} kg/(m·s)
Bulk density[b]	ρ	10^3 kg/m^3
Gibbs elasticity[c]	E	10^{-2} kg/s^2
Interface shear viscosity[c]	η_s	10^{-7} kg/s
Depletion length[c]	$h_\Gamma = \partial\Gamma/\partial c$	10^{-6} m

[a] Here W is the dynamical meniscus width $W_d = \sqrt{Hr_m}$, but larger W values are expected far from the meniscus when thickness gradients are present, as represented in **Figure 2**.

[b] Classical values for aqueous solutions of surfactant.

[c] Commonly encountered values, which may vary significantly with the surfactant solution.

The liquid phase is a Newtonian fluid of density ρ and bulk viscosity η. It is assumed to be a surfactant solution of bulk concentration c_0, surface concentration Γ_0, and surface tension γ_0. We assume that the interfaces are in a liquid state described by the Boussinesq–Scriven model, which accounts for shear and dilatational interface viscosities, η_s and κ_s, respectively. The variation in surface tension $\delta\gamma = \gamma - \gamma_0$ is governed by the Gibbs modulus E, under some restrictions (see Sections 2.3 and 2.5). This modulus depends on the depletion length $h_\Gamma = \partial\Gamma/\partial c$ and the Marangoni modulus $E_M = \Gamma_0 \partial\gamma/\partial\Gamma$, both of which can be determined from the thermodynamic properties of the solution (for a review of these physicochemical properties, see Manikantan & Squires 2020).

2.1. Pressure, Bulk Velocity, and Mass Conservation

In films thicker than 100 nm, the short-range forces responsible for the so-called disjoining pressure are negligible (Stubenrauch & von Klitzing 2003), in contrast with regimes recently addressed, e.g., by Zhang & Sharma (2018), Yilixiati et al. (2019), Shah et al. (2019), and Chatzigiannakis et al. (2020). One of the fundamental properties of thin films is that pressure does not vary across the film thickness. The pressure in the whole film can thus be deduced from the normal stress continuity at the top/bottom interface. Its full expression is given by Edwards et al. (1991, equations 4.2– 20) and Manikantan & Squires (2020), and it is simplified here by taking advantage of the assumptions listed in **Table 1**. The bulk viscous stress associated to the film stretching, of the order of $\eta U_S/W$, and the hydrostatic pressure, of the order of $\rho g H$, are much smaller than the Laplace pressure jump, so the pressure in the film is given by $p(x, y) = -\gamma_0 \Delta h(x, y)$. Δh is an approximation of the top/bottom interface curvature in the limit of small ε, and the reference pressure is taken in the gas phase. Note that this equation remains valid for spherical soap bubbles of radius R_{sph} as long as $W^2/R_{sph}^2 \ll 1$ (Vitry et al. 2019, supplemental equation 10). In that case, the reference pressure is the average between the external and internal gas pressures.

In the central part of the film, if the relevant horizontal length scale W (see **Figure 2**) is the whole film size $R_f \sim 100$ μm, then the pressure is of the order of $\pm\gamma_0 H/R_f^2 \sim \pm 3$ Pa, whereas the meniscus pressure is of the order of $-\gamma_0/r_m \sim -300$ Pa. As a consequence, there is a pressure gradient localized at the transition between the film and the meniscus, in a region denoted as the dynamical meniscus. This is the driving force for the capillary drainage from the film to the meniscus.

The Navier–Stokes equation can be strongly simplified too. Whether the velocity is dominated by U_{S} or U_{P}, the conditions on Re_{P} and $U_{\mathrm{S}}/U_{\mathrm{P}}$ impose that the inertial terms are negligible. The condition $U_{\mathrm{S}}/U_{\mathrm{P}} \ll \varepsilon^{-2}$ (or, equivalently, $U_{\mathrm{S}}/U_{\mathrm{P}}$ at most of the order $1/\varepsilon$, as written in **Table 1**) defines the lubrication regime. It imposes that the z derivatives of the velocity are dominant in the bulk viscous forces. The Stokes equation then becomes $\eta \partial^2 \mathbf{u}/\partial z^2 = \nabla p$. Using the pressure expression given above, it leads to

$$\mathbf{u}(x,y,z) = -\frac{\gamma_0}{\eta}\left(\frac{z^2}{2} - \frac{h(x,y)^2}{2}\right)\nabla(\Delta h)(x,y) + \mathbf{u}_{\mathrm{s}}(x,y) = \mathbf{u}_{\mathrm{p}}(x,y,z) + \mathbf{u}_{\mathrm{s}}(x,y), \tag{1}$$

$$\mathbf{q}(x,y) = \int_0^h \mathbf{u}\,\mathrm{d}z = \frac{\gamma_0}{3\eta}h^3\nabla(\Delta h) + \mathbf{u}_{\mathrm{s}}h = \mathbf{q}_{\mathrm{p}}(x,y) + \mathbf{q}_{\mathrm{s}}(x,y), \tag{2}$$

where $\mathbf{q}$ is the liquid flux integrated over the film half-thickness. The velocity is decomposed into a Poiseuille flow $\mathbf{u}_{\mathrm{p}}$ and a plug flow $\mathbf{u}_{\mathrm{s}}$, leading to the corresponding fluxes $\mathbf{q}_{\mathrm{p}}$ and $\mathbf{q}_{\mathrm{s}}$. The former is driven by the pressure gradient and thus by the interface curvature. Note that from Equation 1, we get the scaling $Ca_{\mathrm{P}} \sim \varepsilon^3$ shown in **Table 1**. The interface velocity scale is more subtle and is discussed in Section 2.2.

The mass conservation equation $\partial h/\partial t = -\nabla \cdot \mathbf{q}$ becomes

$$\frac{\partial h}{\partial t} + \mathbf{u}_{\mathrm{s}} \cdot \nabla h = -\nabla \cdot \left(\frac{\gamma_0}{3\eta}h^3\nabla(\Delta h)\right) - h\nabla \cdot \mathbf{u}_{\mathrm{s}}, \tag{3}$$

where the left-hand-side term is the material time derivative of the thickness of a film element followed along its trajectory. This thickness may decrease/increase because the film element loses/gains some volume due to the Poiseuille flows (first term on the right) or because the film element is stretched/compressed in its plane, while keeping a constant volume (second term on the right).

2.2. Interface Velocity and Capillary Stress Tensor

A second equation coupling h and $\mathbf{u}_{\mathrm{s}}$ can be derived from the tangential stress continuity at the interface, which can be seen as a force balance on the system defined by the magenta box in **Figure 2**. Alternatively, the same equation can be obtained by considering the force balance on a film element, projected in the (x, y) plane. This perspective, adopted in this review, not only defines the net force exerted by surface tension and bulk pressure on the film element, but also introduces the 2D capillary stress tensor $\overset{\Rightarrow}{\sigma}_{\mathrm{cap}}$, representing the force exerted on each of its lateral faces. This formulation establishes a clear analogy between the obtained equation of motion and the 3D Stokes equation.

2.2.1. Capillary stress tensor.

Let us consider a film element of thickness $2h$ and area $\mathrm{d}A$. Among the four lateral faces, each face f has an area $2h\mathrm{d}l_f$ and a normal $\mathbf{e}_{\mathrm{f}}$ [in the (x, y) plane], oriented outward. As an example, for the film element depicted in perspective in **Figure 2**, and for its visible green face, we have $\mathbf{e}_{\mathrm{f}} = \mathbf{e}_{\nabla}$ and $\mathrm{d}l_{\mathrm{f}} = \mathrm{d}s$. The capillary stress tensor $\overset{\Rightarrow}{\sigma}_{\mathrm{cap}}$ is defined such that the force $\mathrm{d}\mathbf{F}_{\mathrm{f}}$ exerted by the external film on the face f is

$$\mathrm{d}\mathbf{F}_{\mathrm{f}} = \overset{\Rightarrow}{\sigma}_{\mathrm{cap}} \cdot \mathbf{e}_{\mathrm{f}}\,\mathrm{d}l_{\mathrm{f}}. \tag{4}$$

Keeping terms up to the order $\gamma_0\varepsilon^2$, we get, as established by Lenavetier et al. (2024, supplemental material), $\overset{\Rightarrow}{\sigma}_{\mathrm{cap}} = [2\gamma_0 h\Delta h + 2\,(\gamma_0 + \delta\gamma)]\overset{\Rightarrow}{I} + \overset{\Rightarrow}{\sigma}{}^{*}_{\mathrm{cap}} = \sigma_{\mathrm{f}}\overset{\Rightarrow}{I} + \overset{\Rightarrow}{\sigma}{}^{*}_{\mathrm{cap}}$, where $\overset{\Rightarrow}{I}$ is the identity tensor. The isotropic term σ_{f} is due to the Laplace pressure $\gamma_0\Delta h$ integrated over the film thickness $2h$ and to the tension $\gamma = \gamma_0 + \delta\gamma$ on each interface.

The tensor $\overset{\Rightarrow}{\sigma}{}^{*}_{\text{cap}}$ is the deviatoric part of the stress tensor. It comes from the second-order corrections of the tension forces, due to projections in the (x, y) plane (see **Figure 2**). It is conveniently expressed in the local basis $\mathcal{B}_e = (\mathbf{e}_\nabla, \mathbf{e}_\perp)$, where $\mathbf{e}_\nabla = \nabla h / |\nabla h|$ follows the thickness gradient and $\mathbf{e}_\perp$ is perpendicular to it, both lying in the (x, y) plane. The corresponding film element, shown in **Figure 2** (inset), has an area $\mathrm{d}A = \mathrm{d}s\, \mathrm{d}\xi$. In this basis and in $\mathcal{B}_0 = (\mathbf{e}_x, \mathbf{e}_y)$ we get

$$\overset{\Rightarrow}{\sigma}{}^{*}_{\text{cap}} = \gamma_0 \begin{pmatrix} -(\nabla h)^2 & 0 \\ 0 & (\nabla h)^2 \end{pmatrix}_{\mathcal{B}_e} = -\gamma_0 \begin{pmatrix} (\partial_x h)^2 - (\partial_y h)^2 & 2\partial_x h\, \partial_y h \\ 2\partial_x h\, \partial_y h & (\partial_y h)^2 - (\partial_x h)^2 \end{pmatrix}_{\mathcal{B}_0}. \qquad 5.$$

A film element is thus submitted to an anisotropic stress, with a higher tensile stress in the direction perpendicular to the thickness gradient. This higher tensile stress can be seen as a tension acting along the boundary between pieces of film of different thicknesses and is denoted as a capillary line tension by Lenavetier et al. (2024). A direct consequence is that a piece of film of a thickness larger (or smaller) than the surrounding film thus relaxes toward a circular pattern. This explains the circular shape of the colored spots easily observed in the flat part of soap films, as well as the hemi-circular shapes at the contact with the meniscus, as seen in **Figure 1*c*,*f*,*g***.

2.2.2. Viscous forces and equation of motion. The capillary force acting on a film element is $\mathbf{F}_{\text{cap}} = \nabla \cdot \overset{\Rightarrow}{\sigma}_{\text{cap}}$ (per unit area of film). It can be easily computed from the expression of σ_{f} and $\overset{\Rightarrow}{\sigma}{}^{*}_{\text{cap}}$ (Equation 5, expressed in $\mathcal{B}_0$) and leads to (twice) the first and last terms in Equation 6. If the film element motion is damped by the interface viscous forces, the capillary force is balanced by the divergence of the viscous stress tensor $[(\kappa_{\text{s}} - \eta_{\text{s}}) \nabla \cdot \mathbf{u}_{\text{s}}] \overset{\Rightarrow}{I} + \eta_{\text{s}} \left[\nabla \mathbf{u}_{\text{s}} + (\nabla \mathbf{u}_{\text{s}})^{\mathrm{T}} \right]$, on each interface. The equation of motion is then

$$\gamma_0 h \nabla(\Delta h) + \eta_{\text{s}} \Delta \mathbf{u}_{\text{s}} + \kappa_{\text{s}} \nabla(\nabla \cdot \mathbf{u}_{\text{s}}) + \nabla \delta\gamma = 0. \qquad 6.$$

This equation, used, e.g., by Bruinsma (1995), is a 2D equivalent of the 3D Stokes equation (see **Table 3**). The term $\nabla \delta\gamma$ is the Marangoni stress, playing an equivalent role as the pressure gradient in three dimensions. The term $\gamma_0 h \nabla(\Delta h)$ has no 3D equivalent. Importantly, this term does not appear as a gradient (due to the contribution of $\overset{\Rightarrow}{\sigma}{}^{*}_{\text{cap}}$) and, in generic situations, cannot be balanced by the Marangoni stress alone. The solutions of Equation 6 have then necessarily nonzero interfacial velocities.

It can be quantified by taking the curl of Equation 6: This keeps only the first two terms, which should balance each other. If the term $\nabla \wedge [\gamma_0 h \nabla(\Delta h)]$ is nonzero (which is the case for randomly chosen thickness fields, the so-called generic cases), it scales as $(\gamma_0 / W^2)\, \varepsilon^2$. This sets the scaling of $\nabla \wedge (\eta_{\text{s}} \Delta \mathbf{u}_{\text{s}})$ and yields $U_{\text{S}} \sim \gamma_0 H^2 / (\eta_{\text{s}} W) \sim 3$ cm/s. In such a situation, the velocity field is typically dominated by the interfacial velocity: $U_{\text{S}} \gg U_{\text{P}}$. For instance, the high velocities observed during the destabilization process shown in **Figure 1** and

Table 3 Analogy between soap film flows and 3D Stokes flows

2D case	3D case
Soap film	3D fluid
Equation 6	Stokes equation
$\mathrm{div}^{2\mathrm{D}} \mathbf{u}_{\text{s}} = \mathrm{d}/\mathrm{d}t(\delta A / A)$	$\mathrm{div}^{3\mathrm{D}} \mathbf{u} = \mathrm{d}/\mathrm{d}t(\delta V / V)$
$\delta\gamma = E/2\, \delta A / A$	$-\delta P = 1/\chi\, \delta V / V$
$\eta_{\text{s}}, \kappa_{\text{s}}$	η, κ
$\gamma_0 h \nabla(\Delta h)$	External force

In the incompressible limit, the 3D/2D velocity divergence tends to zero and the pressure/tension does not depend on the compressibility $(1/\chi)$ or E anymore.

discussed in Section 5 are governed by this simple balance between a capillary force, determined by the thickness field, and viscous resistance.

If the film thickness is axisymmetrical or invariant under translation, an entirely different scenario arises. In these symmetrical cases, the thickness field satisfies $\nabla \wedge [\gamma_0 h \nabla(\Delta h)] = 0$, and solutions with small or negligible interfacial velocities are typically observed: $U_\mathrm{S} \ll U_\mathrm{P}$, in contrast with the generic cases. Such behavior is observed for the axisymmetric drainage situations discussed in Section 4.

Using $Ca_\mathrm{P} = \eta U_\mathrm{P}/\gamma_0 \sim \varepsilon^3$, the scaling obtained for U_S in the generic situation can be reformulated as $Bq U_\mathrm{S}/U_\mathrm{P} \sim 1/\varepsilon^2$. As the validity of the lubrication equations also requires $U_\mathrm{S}/U_\mathrm{P} \leq 1/\varepsilon$, we get the condition $\eta_\mathrm{s} \geq \eta W$, which is satisfied by the interface shear viscosity assumed in **Table 2**, but would not be for $\eta_\mathrm{s} < 10^{-8}$ Pa·s, as found for small soluble surfactants by Zell et al. (2014). In that case, the main damping force is the gas friction, but the same qualitative film flows are expected (Hughes et al. 1981).

Note that the bulk viscous friction on the lateral sides of the film element scales as $\eta U_\mathrm{S} H/W^2 \leq (\gamma_0/W)\varepsilon^3$ and is a priori not large enough to compensate the driving force in the regime of **Table 1**.

Taking the divergence of Equation 6 reveals another relationship: The divergence of the first term, scaling as $\gamma_0 H^2/W^4$, should balance $\Delta[(\eta_\mathrm{s} + \kappa_\mathrm{s})\nabla \cdot \mathbf{u}_\mathrm{s} + \delta\gamma]$, which imposes that $(\eta_\mathrm{s} + \kappa_\mathrm{s})\nabla \cdot \mathbf{u}_\mathrm{s} + \delta\gamma$ scales as $\gamma_0 \varepsilon^2$. The relative contribution of these terms is discussed in Section 2.5.

2.3. A Constitutive Equation for the Tension—Gibbs Elasticity

The surface tension is related to the interface surfactant concentration and its value is thus coupled, for soluble surfactants, to the concentration field in the bulk.

When the interface is stretched, the surfactant concentration decreases at the interface and the tension increases. Soluble surfactants reabsorb from the bulk sublayer until the initial equilibrium state is recovered, so the tension increase is a transient, out-of-equilibrium state (Lucassen-Reynders et al. 2001). However, for thin-enough films, the readsorption of surfactant is able to deplete the volume and to displace the interface/bulk equilibrium toward smaller concentrations. During an experimental time range discussed in Section 2.5, the film elements can be considered as closed systems at equilibrium, and, in this limit, the tension becomes a function of the film extension. The Gibbs elasticity can be defined as (Gibbs 1876)

$$E = 2 \left.\frac{\partial \gamma}{\partial \ln A}\right|_{\Omega} = 2E_M \frac{1}{1 + \frac{h}{h_\Gamma}}, \qquad 7.$$

with A the area of the film element, varied at constant volume Ω around its value A_0 of reference at which, by definition, $\gamma = \gamma_0$. E is defined for a film having two interfaces, hence the factor 2. The surfactant mass conservation leads to the second equality (Mysels et al. 1961, van den Tempel et al. 1965, Couder et al. 1989), which involves the depletion length $h_\Gamma = \partial\Gamma/\partial c$.

The confinement is at the origin of the Gibbs elasticity: In the limit of film thickness much larger than h_Γ, the Gibbs elasticity vanishes; in the thin film limit, the total amount of surfactant in the volume becomes negligible, the surfactant behaves as an insoluble species, and twice the Marangoni modulus E_M is recovered.

The interface area A of a film element followed along its trajectory evolves with time due to the interface velocity divergence. Introducing the deformation $\lambda = (A - A_0)/A_0$, we get $\partial\lambda/\partial t + \mathbf{u}_\mathrm{s} \cdot \nabla\lambda = \nabla \cdot \mathbf{u}_\mathrm{s}$. If the film can be modeled with a Gibbs elasticity, then in the linear regime $\delta\gamma = E\lambda/2$ and

$$\frac{\partial \delta\gamma}{\partial t} + \mathbf{u}_\mathrm{s} \cdot \nabla \delta\gamma = \frac{E}{2} \nabla \cdot \mathbf{u}_\mathrm{s}. \qquad 8.$$

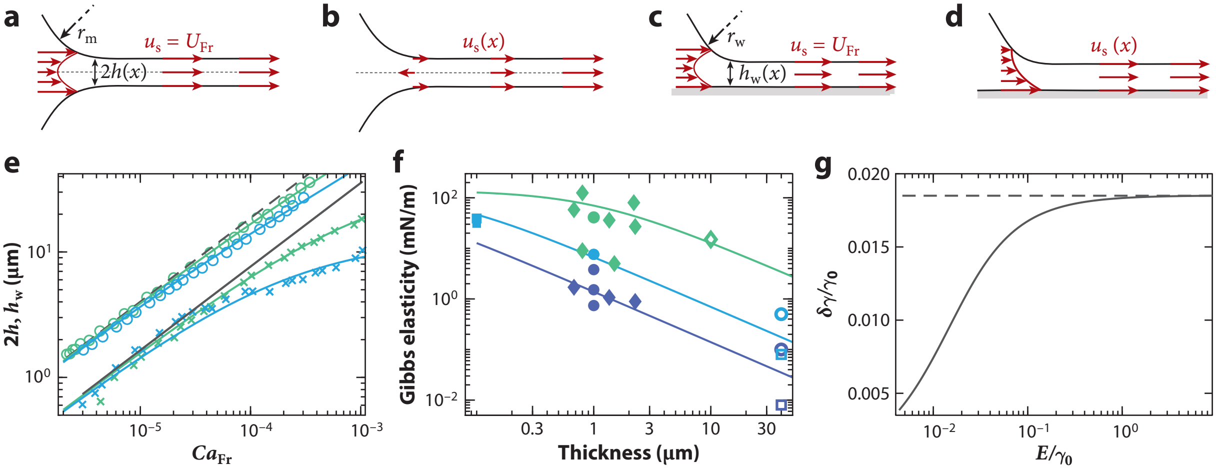

Figure 3

Film extraction at the imposed velocity U_{Fr} and transition from an incompressible to a compressible behavior. (*a*–*d*) Schematic representations of the velocity field for (*a*,*b*) free or (*c*,*d*) supported films, in the (*a*,*c*) incompressible or (*b*,*d*) stress-free limits. (*e*) Soap film thickness $2h$ and wetting film thickness h_w as a function of $Ca_{Fr} = \eta U_{Fr}/\gamma_0$ for $C_{12}E_6$ at 3 CMC (*green*) and 10 CMC (*blue*) (all the data associated to the wetting geometry are shifted vertically by a factor of 2 for readability). The colored lines are the numerical resolution of Equations 3, 6, and 8 with $E/\gamma_0 = 16 \times 10^{-3}$ (*green*) and 5×10^{-3} (*blue*). The gray line is the prediction $2h_{Fr}$ given by Equation 9 and the dashed line is the Landau–Levich prediction $h_w = 4^{2/3} h_{Fr}$, both assuming incompressible interfaces. Panel adapted from Champougny et al. (2015). (*f*) Gibbs elasticities measured by Prins et al. (1967) and Prins & Van den Tempel (1969) on SDS, CTAB, and sodium decane sulfonate (*solid diamonds*); by Georgieva et al. (2009) on $C_{12}E_6$ and $C_{12}G_2$ (*solid squares*); by Poryles et al. (2022) on SDS (*solid circles*); by Pasquet et al. (2022) on TTAB (*hollow squares*); by Zhao & Xu (2024) on Fairy liquid (*hollow diamond*); and by Champougny et al. (2015) on $C_{12}E_6$ (*hollow circles*). For the data at $h = 40$ µm, the thickness is an estimation discussed in the text. The concentration is above 1.2 CMC (*dark blue*), below 0.8 CMC (*green*), or between these limits (*light blue*). The colored lines are Equation 7 for $E_M = 70$ mN/m and $h_\Gamma = 5, 25$, and 500 nm from bottom to top, for illustrative purposes. (*g*) Excess of tension in the film as a function of the elastic modulus for $Ca_{Fr} = 0.33 \times 10^{-3}$. The dashed line shows the upper value $3.84\, Ca^{2/3}$ (see Equation 9) reached at large E. Panel adapted from Seiwert et al. (2014). Abbreviations: CMC, critical micelle concentration; CTAB, cetyltrimethylammonium bromide; SDS, sodium dodecyl sulfate; TTAB, tetradecyltrimethylammonium bromide.

This last equation closes the problem, and the unknowns h, $\mathbf{u}_s$, and $\delta\gamma$ can thus be determined from Equations 3, 6, and 8, if the boundary and initial conditions are known.

2.4. Experimental Determination of the Gibbs Elasticity

Various surface tension measurement techniques have been employed to determine the Gibbs elasticity. In experiments by Mysels et al. (1961), Prins et al. (1967), and Prins & Van den Tempel (1969), a vertical film suspended on a frame is slightly stretched, and the resulting increase in tension is measured using a dynamometer or inferred from the film's weight as a function of thickness, validating the thickness dependency predicted in Equation 7. A soap bubble is swelled in experiments by Bianco & Marmur (1993), Georgieva et al. (2009), and Karakashev et al. (2010), and the surface tension is inferred from the bubble's internal pressure. In experiments by Bussonnière & Cantat (2021) and Poryles et al. (2022), an assembly of soap films undergoes area variations, with tension differences deduced from the motion of the meniscus connecting them.

More indirectly, E can be derived from film extraction experiments (Champougny et al. 2015) or through the propagation of symmetric waves in falling soap films (Zhao & Xu 2024), as originally tried by Tran et al. (2009) and Kim & Mandre (2017).

A summary of these results is presented in **Figure 3*f*** for simple surfactant solutions, highlighting the importance of the film thickness and of the surfactant concentration, which controls the value of h_Γ. For film thicknesses around 1 μm, E may reach 100 mN/m below the critical micelle concentration (CMC), is typically of the order of 10 mN/m around the CMC, and drops to 1 mN/m at larger concentrations, possibly influenced by impurity traces. When a less soluble species, such as dodecanol, is added as cosurfactant at concentration c_{cos}, E increases with c_{cos}, reaching several tens of millinewtons per meter.

Since the Gibbs elasticity is based on the differentiation of γ, it is strictly applicable only for small interface extensions. For large deformations λ, the Marangoni modulus E_{M} and depletion length h_Γ must be replaced by the nonlinear thermodynamic laws $\Gamma(c)$ and $\gamma(c)$ (Prins et al. 1967). Experimentally, $\gamma(\lambda)$ is well-approximated by the empirical relation $\gamma_0 + (E^{\mathrm{eff}}/2)\lambda/(1+\lambda)$ with E^{eff} a fit parameter (Poryles et al. 2022).

2.5. Limitations of the Model

The limitations of the model can be illustrated with the case of the axisymmetric drainage of a film of radius R_{f} trapped at $t = 0$ between two bubbles that impose a meniscus pressure $-\gamma_0/r_{\mathrm{m}}$. As soon as the bubbles are deformed, the trapped film is submitted to a tensile stress, as is shown in the examples in Section 4. In response to this external forcing, the film stretching may be limited by (*a*) the inertia, (*b*) the bulk viscous stress, or the interface stress dominated by (*c*) the Marangoni stress or (*d*) the interface viscous stress.

Cases *a* and *b* correspond to the extensional regime and are ruled by a different set of equations than the ones discussed in Section 2. Case *a* is addressed by Chesters & Hofman (1982) for film drainage and by, e.g., Chomaz (2001), Kellay (2017), and Motaghian et al. (2019) for other geometries. In case *b*, discussed by Howell & Stone (2005), Ilton et al. (2016), Bartlett et al. (2023), and Eshima et al. (2024), the film thickness is shown by Breward & Howell (2002) to remain uniform during drainage and to decrease as $r_{\mathrm{m}}[\eta R_{\mathrm{f}}/(\gamma_0 t)]^2$. The film collapses in a fraction of a second for usual viscosities.

Cases *c* and *d* correspond to the lubrication regime covered by this review. Let us consider first the case (*c*) of negligible intrinsic interface viscosities. The external tensile stress then imposes the tension increase $\delta\gamma$ and thus the film extension λ. The timescale needed to equilibrate the concentrations between the interface of the film element and its bulk is, if limited by the diffusion, $\tau_\perp \sim H^2/D \sim 10$ ms, where D is the diffusion coefficient of the order of 10^{-10} m^2/s. For $t \ll \tau_\perp$, the extension is governed by the Marangoni elasticity $E_{\mathrm{M}} > E$ and $\lambda = \delta\gamma/E_{\mathrm{M}}$. Then λ increases at a rate controlled by the surfactant adsorption, until it reaches $\lambda = \delta\gamma/E$. The transverse diffusion thus leads to an effective dilatational viscosity that may control the film stretching at these short timescales (Lucassen-Reynders et al. 2001, Mezache et al. 2024).

Similarly, the in-plane diffusion occurs on the timescale $\tau_\parallel \sim W^2/D \sim 1$–100 s for the typical values of W between 10 and 100 μm. For times larger than $\tau_\parallel$, the in-plane transport becomes nonnegligible, the assumption of a closed film element fails, and Equation 7 is not valid anymore. The surfactant flux toward the film leads to interface creation and to film extension. This diffusive process once again leads to an effective dilatational viscosity, which becomes dominant over the Gibbs elasticity at large timescales. Convective transport due to Poiseuille flow can also invalidate the assumption that the film element behaves as a closed system (Seiwert & Cantat 2015).

The Gibbs elasticity is thus a relatively weak concept, with a restricted range of validity imposing experimental timescales between $\tau_\perp$ and $\tau_\parallel$. Recent numerical simulations (Dai & Leal 2008, Titta et al. 2018, Vitry et al. 2019, Atasi et al. 2020, Shi et al. 2022, Lian et al. 2024) take into account the whole convection/diffusion transport of surfactant (in bulk or at the interface only) and thus address ranges of Péclet numbers $Pe = WU_{\mathrm{S/P}}/D$ not accessible with the Gibbs elasticity formalism. However, when applicable, the Gibbs elasticity provides a simple and useful relationship between tension and interface deformation.

When the Gibbs elasticity is well-defined and nonvanishing, it usually dominates the film extension over the intrinsic interface viscosity, as experimentally observed by Hermans et al. (2015) and Bussonnière & Cantat (2021). Indeed, from Equation 8, an extensional interface velocity field lasting during a timescale τ^{exp} generates an overtension $\delta\gamma \sim \tau^{\mathrm{exp}} E \nabla \cdot \mathbf{u}_{\mathrm{s}}$. It dominates $\kappa_{\mathrm{s}} \nabla \cdot \mathbf{u}_{\mathrm{s}}$ in Equation 6 if $\kappa_{\mathrm{s}} \ll \tau^{\mathrm{exp}} E$. For vanishingly small Gibbs elasticities, the extensional regimes *a* or *b* rather than *d* are usually observed, unless the Boussinesq number (based on dilatational viscosity) is very large.

The transition between the extensional and lubrication regimes is addressed by Münch et al. (2005) in the context of wetting films.

3. A FIRST EXAMPLE: PULLING A SOAP FILM OUT OF A MENISCUS

The extraction of a film from a soapy solution has been extensively studied, both theoretically and experimentally in the frame of the model discussed in Section 2. In this section, we use this example to illustrate some general properties of soap films that, within certain limits, apply to many other geometries.

3.1. The Frankel Film

When a rectangular frame is pulled out of a soapy solution at a constant velocity U_{Fr}, a film, denoted as the Frankel film, is extracted from the meniscus at the bottom (Mysels et al. 1959). This process, typically studied in vertical setups (Mysels & Cox 1962, Lionti-Addad & Di Meglio 1992, Cohen-Addad & di Meglio 1994, Lal & di Meglio 1994, Adelizzi & Troian 2004, Berg et al. 2005, van Nierop et al. 2008, Saulnier et al. 2011), is independent of gravity (which only determines the meniscus curvature $1/r_{\mathrm{m}} = \sqrt{2\rho g/\gamma_0}$ at the contact with the film) and occurs similarly in horizontal films (Seiwert et al. 2013, Petit et al. 2015).

The film extraction mechanism becomes clearer when the frame is partially immersed at time $t = 0$, with a film already present on the upper part of the frame. As the frame begins to move upward with velocity U_{f}, it stretches the film, thereby increasing its tension. This increased film tension exerts a pulling force on the meniscus interfaces, which begin to slide toward the film at a velocity $U_{\mathrm{Fr}} < U_{\mathrm{f}}$. This motion drags foaming solution into the film region, working against the meniscus's capillary suction and resulting in the formation of the extracted film.

During this transient, the film extension rate is given by $\mathrm{d}\lambda/\mathrm{d}t = (U_{\mathrm{f}} - U_{\mathrm{Fr}})/L_{\mathrm{film}}$, where L_{film} denotes the vertical extent of the film. A steady state is reached when the film tension, which increases with the extension λ, becomes sufficient to extract film from the meniscus at a rate matching the frame velocity. The steady state condition is thus $U_{\mathrm{Fr}} = U_{\mathrm{f}}$ and $\mathrm{d}\lambda/\mathrm{d}t = 0$.

The key observable is the film half-thickness extracted in this steady regime. As shown in **Figure 3*e***, it increases with $Ca_{\mathrm{Fr}} = \eta U_{\mathrm{Fr}}/\gamma_0$, and at large velocities, it also increases with the Gibbs elasticity, which determines the ability of the interface to overcome the capillary suction. This behavior is reproduced in solutions of Equations 3, 6, and 8 by Champougny et al. (2015).

In this work, the Gibbs modulus E is a fitting parameter and the obtained values are compatible with the direct measurements of E if the average thickness in the dynamical meniscus, estimated as 40 ± 10 μm, is used (see **Figure 3*e*,*f***).

The models also provide insights into nonmeasurable quantities, particularly the surface tension. Tension remains uniform in the meniscus (γ_0) and in the film ($\gamma_0 + \delta\gamma$) but varies sharply across the dynamical meniscus (Seiwert et al. 2014). At a fixed capillary number Ca_{Fr}, the tension difference between the film and the meniscus increases with E and eventually saturates at a maximal value for a critical Gibbs elasticity $E^* \propto \gamma_0 Ca_{\mathrm{Fr}}^{2/3}$, as shown in **Figure 3*g***. Above E^*, E becomes large enough to prevent interface extension, making $\delta A/A$ negligible but still decreasing proportionally to $1/E$. At the same time, the tension difference $\delta\gamma = (E/2)\delta A/A$ reaches a plateau and becomes independent of E. The highest Marangoni stress is thus reached at large E, when the interface extension vanishes. There is an exact parallel, summarized in **Table 3**, between this limit and the bulk incompressibility limit in a 3D fluid.

In this incompressible interface regime, the Gibbs elasticity scales out of the problem, the interface velocity is uniformly equal to the imposed velocity U_{Fr}, and all the half-film thicknesses measured in **Figure 3*e*** converge toward the same master curve, denoted as the Frankel solution (Mysels et al. 1959), for which

$$h_{\mathrm{Fr}} = 1.33\, r_{\mathrm{m}} \left(\frac{\eta U_{\mathrm{Fr}}}{\gamma_0}\right)^{2/3} \quad \text{and} \quad \delta\gamma_{\mathrm{Fr}} = 3.84\, \gamma_0 \left(\frac{\eta U_{\mathrm{Fr}}}{\gamma_0}\right)^{2/3} = 2.89\, h_{\mathrm{Fr}} \frac{\gamma_0}{r_{\mathrm{m}}}. \qquad 9.$$

3.2. Limit of Incompressible Interfaces

At a large Gibbs modulus, the interface extension or compression becomes negligible, and a simplified model can be used, denoted as the incompressible interface model (IIM). It is shown to very efficiently reproduce the flows observed in thin liquid films for many surfactant solutions and many external conditions.

3.2.1. General remarks. In the model previously developed, the tension is given by $\delta\gamma = (E/2)\delta A/A$, or equivalently by Equation 8. When the incompressible interface limit is reached, these equations are replaced by $\nabla \cdot \mathbf{u}_{\mathrm{s}} = 0$, and $\delta\gamma$ becomes the Lagrange multiplier enforcing this incompressibility condition (Manikantan & Squires 2020, section 3.3.2). Then, given a thickness field and boundary conditions at the film rim, Equation 6, coupled to $\nabla \cdot \mathbf{u}_{\mathrm{s}} = 0$, fully determines $\mathbf{u}_{\mathrm{s}}$ and $\delta\gamma$ without extra input.

However, the relation $\delta\gamma = (E/2)\delta A/A$ remains valid and can be used to validate a posteriori the assumption of interface incompressibility. The incompressibility condition states that $\delta A = 0$, so $\delta A/A$ must be considered here as a higher-order term in the model, which is deduced from the leading-order equations.

A practical approach is to assume interface incompressibility, to compute $\delta\gamma$ using the simplified equations of motion, and to deduce the area variations from $\delta A/A = 2\delta\gamma/E$. If $\delta A/A$ is below an acceptable threshold (typically $<1\%$ for a required accuracy of the order of 1%), the assumption holds; otherwise, interface compressibility must be considered.

In the example of the Frankel film, the tension $\delta\gamma_{\mathrm{Fr}}$ given by Equation 9 is the solution obtained for the IIM and is thus valid if $\delta A/A \sim \delta\gamma_{\mathrm{Fr}}/E \sim (\gamma_0/E)Ca_{\mathrm{Fr}}^{2/3} \ll 1$. This is the same condition as the condition $E \gg E^*$ obtained by solving the whole problem.

For larger pulling velocities or smaller Gibbs elasticities, the external forcing becomes too high for the interface to resist without extension, and the interfaces stretch, as directly observed by Seiwert et al. (2013), Petit et al. (2015), and Pasquet et al. (2023). In this regime, the extracted film is thinner than the prediction h_{Fr}.

3.2.2. Specificity of the 1D case. Problems with high symmetry simplify further. For flows invariant in the y direction, the condition $\nabla \cdot \mathbf{u}_{\mathrm{s}} = 0$ reduces to $\partial u_{s,x}/\partial x = 0$, implying a uniform interface velocity U_{s}. The same applies to axisymmetric solutions, both referred to as 1D flows.

This uniformity of $\mathbf{u}_{\mathrm{s}}$ is often termed the rigid condition, though its physical origin lies in a sufficiently high Gibbs elasticity—a rheological property analogous to the compression modulus in a 3D fluid (see **Table 3**). Indeed, incompressible interfaces behave as rigid in one dimension, but if the symmetry is broken, they can easily flow, damped by shear interface viscosity (see Section 5). Mysels et al. (1959) use "mobile" to refer to low shear interface viscosity and "rigid" to high shear interface viscosity, with incompressible interfaces in both cases. With these definitions, rigid and mobile interfaces are indistinguishable in 1D flows.

The velocity U_s is reminiscent of the slip velocity used in the context of wetting films. However, the condition determining U_s in foam films is not local as is the Navier condition [unless an actual slip between the bulk liquid and the surfactant monolayer is considered (Joly et al. 2014)]. By contrast, the velocity U_s is governed by the condition at the boundary of the film, in the (x, y) plane, where the velocity is imposed by the presence of a meniscus, a solid frame holding the film, or any external flow.

These 1D flows with incompressible interfaces are the most extensively studied theoretically and numerically in the literature. In this limit, the equation of motion, Equation 3, involves a single unknown function h and the parameter U_s,

$$\frac{\partial h}{\partial t} + U_s \frac{\partial h}{\partial x} = -\frac{\gamma_0}{3\eta}\frac{\partial}{\partial x}\left(h^3 \frac{\partial^3 h}{\partial x^3}\right). \qquad 10.$$

The Marangoni stress is given by Equation 6, which becomes

$$\frac{\partial \delta\gamma}{\partial x} = -\gamma_0 h \frac{\partial^3 h}{\partial x^3}. \qquad 11.$$

In this regime, the flows are identical to those observed in wetting films (see the sidebar titled Analogies Between Soap Films and Wetting Films) or in simple fluid films trapped between two

ANALOGIES BETWEEN SOAP FILMS AND WETTING FILMS

The equation of motion for 1D flows in soap films with incompressible interfaces is formally identical to the equation governing the flow on a solid wall. Two analogies can be made; they are illustrated in **Figure 3**.

Soap Films and Wetting Films, Both with Incompressible Interfaces

In this case, one interface of the soap film corresponds to the free interface of the wetting film and the other to the wall (**Figure 3*a*,*c***). The evolution of the wetting film thickness h_w is ruled by Equation 10, in which the parameter $\gamma_0/(3\eta)$ is replaced by $\gamma_0/(12\eta)$ (Champougny et al. 2015). A wetting film pulled out of a meniscus of radius r_m at the velocity U_{Fr} is $h_{LL} = 4^{2/3} h_{Fr}$. This is the so-called Landau–Levich problem.

The transition between incompressible and compressible interface behaviors occurs at the same capillary number for the Frankel and Landau–Levich cases, as shown in **Figure 3*e***. However, once interface compressibility becomes significant, the two cases diverge.

In a foam film, both interfaces stretch, leading to a film whose thickness saturates at large U_{Fr}. The extensional regime is eventually reached at very small E (see **Figure 3*b***). In contrast, in the Landau–Levich geometry, the wall still resists extension (see simulation by Champougny et al. 2017) (see **Figure 3*d***). After a transient regime at intermediate capillary numbers, the wetting film thickness satisfies $h_w = h_{Fr}$ and the $Ca_{Fr}^{2/3}$ scaling is recovered (Shen et al. 2002).

Soap Films with Incompressible Interfaces and Wetting Films with Stress-Free Interfaces

Another useful analogy can be drawn by considering only one half of the soap film. In this case, the incompressible film interface is identified with the wall, moving at the velocity U_s, while the symmetry plane $z = 0$ of the film is identified with the free interface of the wetting film, where the stress-free condition leads to the same condition $\partial u_x/\partial z = 0$ (see **Figure 3*a*,*d***). The wetting film thickness h_w thus obeys the same Equation 10 as the soap film half-thickness h.

As a result, all theoretical findings derived for wetting films in the stress-free limit can be directly applied to soap films in the incompressible interface limit [see, e.g., the review by Cantat (2013) for films flowing in or out of a meniscus and the capillary leveling solutions established by McGraw et al. (2012) and Benzaquen et al. (2013)].

highly viscous drops. In these cases, the tangential stress at the interface is generated by the solid wall or the viscosity of the external phase (Leal 2004), rather than by the Marangoni stress in the surfactant layer.

4. AXISYMMETRIC CAPILLARY DRAINAGE AND OTHER 1D FLOWS

The problem of thin film drainage is extensively addressed in reviews by Chan et al. (2011) and Chatzigiannakis et al. (2021). One point of divergence between these two reviews is the relevance of the simple Reynolds drainage law (as defined in Section 4.1.3) in analyzing the thinning dynamics of the film trapped between two bubbles. Here we propose other paradigmatic flows that should be promoted as simple analytical alternative models to interpret experimental data and guide numerical modeling.

The solutions we discuss below are asymptotic laws obtained using the IIM, without disjoining pressure. They are thus insensitive to the initial film shape and to the nature of the foaming solution. However, they lead in many cases to a surprisingly good agreement with experimental data.

When an influence of the foaming solution formulation is observed, they may still be used as efficient benchmarks, in an attempt to identify the origin of this influence, particularly during the initial stage of drainage, where the signature of the interface rheological properties is not obscured by short-range forces associated with the disjoining pressure.

Importantly, for each flow, we provide the associated tension variation $\delta\gamma$, allowing the incompressibility assumption to be quantitatively questioned, as discussed in Section 3.2.

4.1. Some Reference Solutions in the Incompressible Interface Limit

In this section, except in Section 4.1.1, we consider a film of radius R_f, bounded by a circular meniscus. In such axisymmetric situations, the interface velocity must be zero at the symmetry axis. Consequently, the condition of uniform velocity established in Section 3.2.2 enforces a zero interface velocity across the entire film, $U_\mathrm{s} = 0$. In this case, the assumption of incompressible interfaces simplifies to the very simple assumption of immobile interfaces.

The equation of motion, Equation 10, has been established in Cartesian coordinates and needs, in a general case, to be adapted to the axisymmetric geometry (see, e.g., Chan et al. 2011). However, if R_f is large enough, Equation 10 remains valid in the dynamical meniscus, with $x = R_\mathrm{f} - r$ a local coordinate (see **Figure 4*a***).

In the static meniscus, far from the film, the pressure is uniform, and its curvature κ (defined as the sum of the two principal curvatures) is uniform too, and denoted $1/r_\mathrm{m}$. In order to determine the static meniscus shape, which imposes the boundary condition for the flow in the film (see **Figure 4*a*,*b***), the nonlinear expression of the curvature κ must be used:

$$\kappa(r) = \frac{h''}{(1 + h'^2)^{3/2}} + \frac{h'}{(r(1 + h'^2)^{1/2})}. \qquad 12.$$

In the dynamical meniscus, we have $h' \ll 1$, and at large r, we recover $\kappa \approx h''$ and $p = -\gamma_0 h''$ still holds.

4.1.1. Capillary leveling.

Capillary leveling governs the film thickness evolution far from the meniscus. It has mainly been studied in the context of stress-free wetting films but also applies to soap films (see the sidebar titled Analogies Between Soap Films and Wetting Films). Self-similar solutions have been established for the evolution of a bump (or a groove) of initial height and width $h_\mathrm{cl}(0)$ and $w_\mathrm{cl}(0)$ in a soap film of thickness $2h_\infty$ (Benzaquen et al. 2013), leading to

$$w_\mathrm{cl}(t) \sim h_\infty \left(\frac{\gamma_0 t}{\eta h_\infty}\right)^{1/4} \quad \text{and} \quad h_\mathrm{cl}(t) \sim \frac{h_\mathrm{cl}(0) w_\mathrm{cl}(0)}{w_\mathrm{cl}(t)} = \frac{h_\mathrm{cl}(0) w_\mathrm{cl}(0)}{h_\infty} \left(\frac{\gamma_0 t}{\eta h_\infty}\right)^{-1/4}. \qquad 13.$$

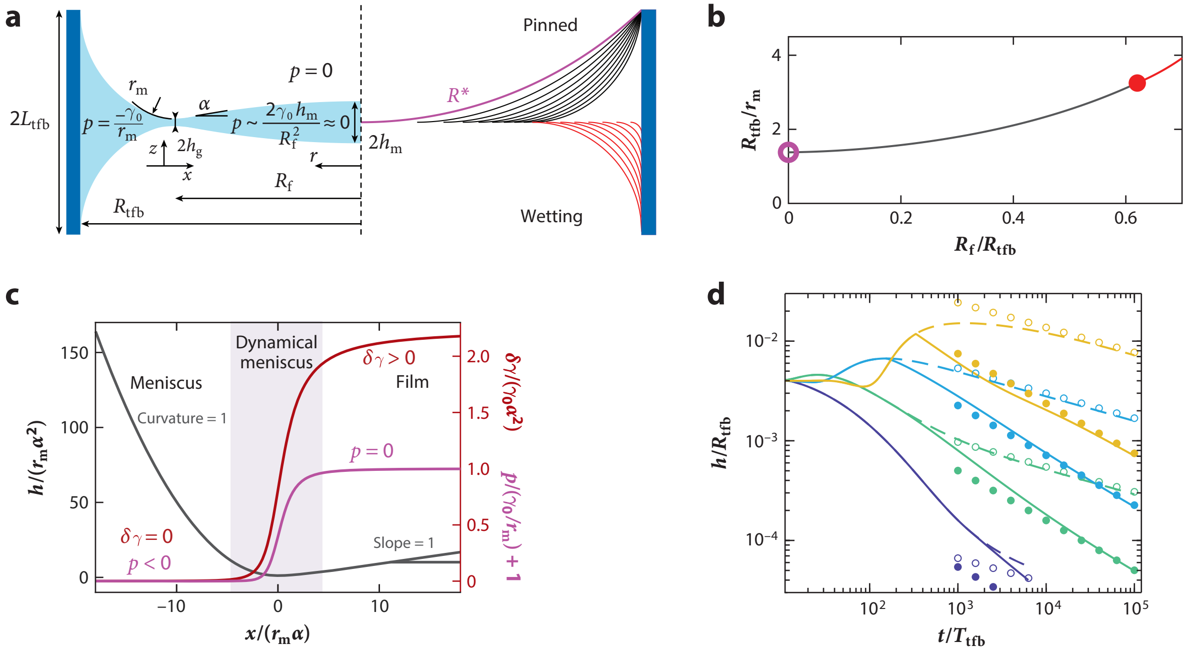

Figure 4

Example of film drainage in thin film balance geometry. (*a*, *left*) Schematics of the dimple and notations used in the text. (*Right*) Numerical solution of Equation 12 for different curvatures $\kappa = 1/r_m$. The conditions are $L_{\text{tfb}}/R_{\text{tfb}} = 0.4$ and a pinned contact line at the cell edge (*black*) or a wetting condition (*red*). The light purple line is the spherical cap of radius $R^* = (L_{\text{tfb}}^2 + R_{\text{tfb}}^2)/(2L_{\text{tfb}})$ obtained when $R_f = 0$. (*b*) Absolute value of the meniscus pressure divided by γ_0/R_{tfb} as a function of the nondimensional film radius R_f/R_{tfb} [numerical results for the pinned case (*gray*) and analytical expression given in Section 4.2 for the wetting case (*red*)]. (*c*) Rescaled film thickness, film tension, and film pressure (with a vertical shift of 1) obtained by numerical solution of Equations 10 and 11 for the groove geometry, as defined in Section 4.1.2. Panel adapted from Frankel & Mysels (1962) and Aradian et al. (2001). (*d*) Dimple maximal (*dashed lines*) and minimal (*full lines*) thicknesses obtained numerically in figure A4 in Chatzigiannakis et al. (2021) as a function of time, for $L_{\text{tfb}}/R_{\text{tfb}} = 0.2$. From bottom to top Ca_{tfb} equals [0.01, 0.04, 0.16, 0.64], where $Ca_{\text{tfb}} = \Delta P R_{\text{tfb}}/\gamma_0$, $\Delta P = \gamma_0/r_m - 2\gamma_0/R^*$ (the meniscus under pressure with respect to the reference situation at $R_f = 0$), and $T_{\text{tfb}} = \Delta P/\eta$. The filled and open symbols are the predictions of Equation 15, with $t_0 = 0$. The radius r_m is deduced from Ca_{tfb}, and R_f is taken from figure A3 in Chatzigiannakis et al. (2021). Panel adapted with permission from Chatzigiannakis et al. (2021).

Similarly, the evolution of a thickness step δh, between h_1 at $x < 0$ and $h_1 + \delta h$ at $x > 0$, is addressed by Aradian et al. (2001) (for $h_1 = 0$) and McGraw et al. (2012). The width of the transition from one thickness to the other scales as $\delta h[\gamma_0 t/\eta\delta h]^{1/4}$. If $\delta h \sim 300$ nm, the transition width reaches 100 μm after approximately 100 s: A well-defined thickness step can thus persist in a soap film for several seconds, as commonly observed.

4.1.2. Groove shape between a film and a meniscus. The evolution of a film in contact with a meniscus is illustrated in **Figure 4**. As discussed in Section 2.1, over the dynamical meniscus, the pressure varies from a value close to zero in the nearly flat film to a lower pressure, $-\gamma_0/r_m$, in the meniscus. The resulting capillary suction leads to a thinning process at the boundary between the meniscus and the film, causing the appearance of a groove along the meniscus, denoted as a barrier rim by Chan et al. (2011) and a pinch by Aradian et al. (2001).

Importantly, if the meniscus mean curvature $1/r_m$ and the slope α of the profile at the connection between the groove and the film remain constant (see **Figure 4**), a steady thickness profile is rapidly reached, with length scales governed by α and r_m. If $U_s = 0$ in the frame of the meniscus, Equation 10 can be integrated into $h^3\,\partial^3 h/\partial x^3 = 3\eta\, q_{\mathrm{g}}/\gamma_0$, where $2q_{\mathrm{g}}$ is the flux (per unit length in the y direction, and counted positively from the meniscus to the film). It is constant and uniform by the assumption of steady state.

All the profiles $h(x)$ solving this equation, and the associated flux q_{g}, can be deduced from the master curve S, plotted in **Figure 4*c*** (Frankel & Mysels 1962, Aradian et al. 2001). S is the solution of $S^3 S''' = -1.21$ and $h(x) = r_{\mathrm{m}}\alpha^2 S(x/(r_{\mathrm{m}}\alpha))$. The thickness length scale is thus $H = r_{\mathrm{m}}\alpha^2$ and the horizontal one $W_{\mathrm{d}} = r_{\mathrm{m}}\alpha$. W_{d} is the characteristic width of the dynamical meniscus and scales as $\sqrt{Hr_{\mathrm{m}}}$, as expected.

Important properties of this solution are the minimum half-thickness in the groove h_{g}, the flux in the half-film q_{g}, and the overtension in the film $\delta\gamma_{\mathrm{g}}$:

$$h_{\mathrm{g}} = 1.52 r_{\mathrm{m}}\alpha^2,\quad q_{\mathrm{g}} = -0.14\frac{\gamma_0}{\eta}\frac{h_{\mathrm{g}}^{5/2}}{r_{\mathrm{m}}^{3/2}},\quad \text{and}\quad \delta\gamma_{\mathrm{g}} = 1.45\frac{\gamma_0}{r_{\mathrm{m}}}h_{\mathrm{g}}. \qquad 14.$$

The groove volume (per unit groove length) scales as $\Omega_{\mathrm{g}} \sim h_{\mathrm{g}} W_{\mathrm{d}} \sim r_{\mathrm{m}}^2\alpha^3$ and adapts to the variations of the external conditions in a time $\tau_{\mathrm{g}} = \Omega_{\mathrm{g}}/q_{\mathrm{g}} \sim \eta\, r_{\mathrm{m}}^2/(\gamma_0 h_{\mathrm{g}})$. With the parameters of **Table 2**, we get $\tau_{\mathrm{g}} = 0.3$ ms. If the relative variations of α and r_{m} occur on timescales larger than τ_{g}, the assumption of steadiness is valid, and the solution simply follows the variation of the external conditions (Etienne-Simonetti et al. 2024).

The meniscus is usually assumed at equilibrium, which imposes r_{m} (see **Figure 4*b***). The slope α depends on the film, which may be at equilibrium, for a small enough film diameter (see Section 4.1.3), or ruled by the capillary leveling (see Section 4.1.1).

4.1.3. Dimple drainage. The tension and the pressure profiles in the groove, plotted in **Figure 4*c***, are uniform in the meniscus and in the film, and they only significantly vary across the dynamical meniscus. If $R_{\mathrm{f}} \gg W_{\mathrm{d}}$, the central part of the film is decoupled from the groove dynamics and relaxes by capillary leveling toward a shape of uniform pressure: It forms a spherical cap, known as a dimple (see left side of **Figure 4*a***). The groove flux q_{g} given by Equation 14 slowly empties and flattens it, thus reducing the angle α, which in turn reduces q_{g} and slows down the drainage.

The dimple volume is $\Omega = \pi h_{\mathrm{m}} R_{\mathrm{f}}^2/2$, where $h_{\mathrm{m}} \ll R_{\mathrm{f}}$ is the maximum half-thickness of the dimple, and the slope α at $r = R_{\mathrm{f}}$ is $\mathrm{d}h/\mathrm{d}x(R_{\mathrm{f}}) = 2h_{\mathrm{m}}/R_{\mathrm{f}}$. If R_{f} is constant, the mass conservation imposes $\mathrm{d}\Omega/\mathrm{d}t = -2\pi R_{\mathrm{f}} q_{\mathrm{g}}(\alpha, r_{\mathrm{m}})$. This leads to, using Equation 14 (Frankel & Mysels 1962, Lin & Slattery 1982),

$$h_{\mathrm{m}} = 0.26\, R_{\mathrm{f}}\sqrt{\frac{R_{\mathrm{f}}}{r_{\mathrm{m}}}}\left(\frac{\gamma_0(t-t_0)}{\eta r_{\mathrm{m}}}\right)^{-1/4},\qquad h_{\mathrm{g}} = 0.42\, R_{\mathrm{f}}\left(\frac{\gamma_0(t-t_0)}{\eta r_{\mathrm{m}}}\right)^{-1/2}. \qquad 15.$$

Note that the minimal half-thickness h_{g} at the boundary of a dimple is almost equal to the Reynolds prediction $h_{\mathrm{g}}^{\mathrm{Rey}} = 0.43R[\gamma_0 t/(\eta r_{\mathrm{m}})]^{-1/2}$, the half-thickness of the liquid sheet trapped between two flat, rigid disks of radius R in contact with the outside negative pressure $-\gamma_0/r_{\mathrm{m}}$ (Chatzigiannakis et al. 2021).

The thickness predictions in Equation 15 are in quantitative agreement with the direct numerical simulations of Chatzigiannakis et al. (2021), as shown in **Figure 4*d***. These asymptotic laws only become exact after a transient regime, which depends on the initial conditions.

In the case of a meniscus in contact with a large film of uniform half-thickness h_∞, the slope α is controlled by the capillary leveling, which leads to the groove time evolution laws established by Aradian et al. (2001).

4.1.4. Moving meniscus. The outer problem is rarely steady, and the film radius may evolve. In that case, and still for incompressible interfaces, the interface velocity is zero in the laboratory frame but not in the meniscus frame, making the groove dynamics of Section 4.1.2 invalid.

In the meniscus frame, with x oriented toward the film and $x = 0$ at the boundary between the meniscus and the film (see **Figure 4**), the interface velocity is $U_\mathrm{s} = \mathrm{d}R_\mathrm{f}/\mathrm{d}t = \dot{R}_\mathrm{f}$. If $\dot{R}_\mathrm{f} > 0$, the geometry of the film extraction discussed in Section 3.1 is recovered. For constant, or slowly varying, meniscus velocity and curvature, the steady solution given by Equation 9 remains valid at each time, and the thickness at $x = 0$ is given by the Frankel solution,

$$h(0,t) = 1.33\, r_\mathrm{m}(t) \left(\frac{\eta \dot{R}_\mathrm{f}(t)}{\gamma_0} \right)^{2/3}. \qquad 16.$$

This extracted film is then advected away from the meniscus while keeping its initial thickness. In this scenario, a film that is thinner near the meniscus than further into the film is simply a signature of a decreasing meniscus velocity.

The film thickness at the meniscus may thus be governed either by $h_\mathrm{g}(t)$ given in Equation 15 for a constant film radius or by Equation 16 for an increasing film size. In the limit of a small $\dot{R}_\mathrm{f}$, a smooth transition between both rules is obtained, the observed thickness being roughly the thickest of both predictions. Similar predictions exist for a decreasing film radius (Cantat 2013).

4.2. Experimental Setups

The drainage of thin films has been studied in various geometries, leading to different external conditions imposed on film, especially the capillary suction. The drop collision (Leal 2004) and bubble collision (Biance et al. 2011) are intrinsically unsteady and have been used to investigate coalescence.

The thin film balance (Sheludko 1967, Sonin et al. 1993), or its bicycle wheel variant (Pereira et al. 2001), offers very practical access to the interfaces: both optically, for measuring the film thickness field, and mechanically, for depositing insoluble surfactants on the two interfaces (Chatzigiannakis & Vermant 2024). Film drainage in this geometry is illustrated in **Figure 4**. The meniscus is usually assumed to be at a uniform pressure, in which case the meniscus pressure can be deduced from the film radius R_f. The black meniscus shapes shown in **Figure 4*a*** are obtained for a meniscus pinned at the hole edge. The corresponding meniscus pressure, in its nondimensional form $R_\mathrm{tfb}/r_\mathrm{m}$, with R_tfb the cell radius, is shown in **Figure 4*b***. It depends on $R_\mathrm{f}/R_\mathrm{tfb}$ and on $L_\mathrm{tfb}/R_\mathrm{tfb}$, where $2L_\mathrm{tfb}$ is the cell thickness. Above a critical R_f value, the meniscus can no longer remain pinned at the edge cell. In this unpinned regime, for a wetting condition at the cell wall, a vertical force balance on the half-meniscus leads to the exact expression $R_\mathrm{tfb}/r_\mathrm{m} = 2R_\mathrm{tfb}^2/(R_\mathrm{tfb}^2 - R_\mathrm{f}^2)$ (Toshev & Ivanov 1975).

Direct measurements of the bubble pressure have been carried out for films trapped between a bubble and a free interface, as reported by Frostad et al. (2016). In this configuration, the geometrical characteristics of the bubble are detailed by Toba (1959), Princen (1963), Lhuissier & Villermaux (2012), and Puthenveettil et al. (2018). The bubble radius r_b is defined from its volume $4\pi r_\mathrm{b}^3/3$. For $r_\mathrm{b} \ll \sqrt{\gamma_0/(\rho g)}$, the dry skeleton of the film is a spherical cap of radius $R_\mathrm{cap} = 2r_\mathrm{b}$, and the pressure difference between the meniscus and the film is $-\gamma_0/r_\mathrm{b}$. The solutions given in Section 4.1 for a flat dry skeleton can thus be used by setting $r_\mathrm{m} = r_\mathrm{b}$.

For larger deformations, the boundary conditions for the film are deduced from the bubble deformation by Carnie et al. (2005). Holding the bubble on an atomic force microscope tip leads to very precise force measurements (Dagastine et al. 2006), recently coupled to film thickness measurements by Liu et al. (2018).

At a larger scale, bubble assemblies held on deformable frames have been used to trigger spontaneous film formation by Durand & Stone (2006) and Biance et al. (2009), or to stretch films by

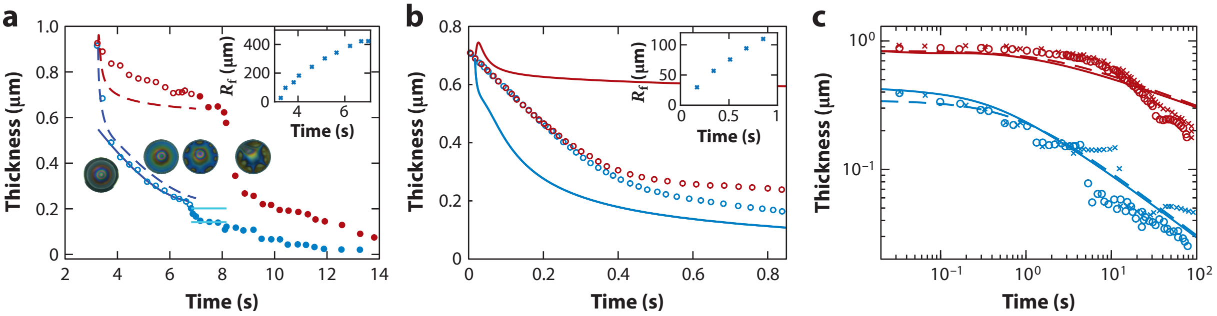

Figure 5

Examples of film drainage, quantified by the minimum and maximum thickness values $2h_{\mathrm{min}}$ (*blue*) and $2h_{\mathrm{max}}$ (*red*). (*a*) Solution of sodium dodecyl sulfate at a concentration of 10 mM, rising bubble. The symbols indicate experimental data from Frostad et al. (2016). The film radius R_{f} increases from $t_0 = 3.2$ s to $t_{\mathrm{m}} = 6.7$ s (*open symbols* and *inset*) and then stabilizes (*solid symbols*). The blue line is a prediction of Equation 16 with $r_{\mathrm{m}} = (3V_{\mathrm{b}}/4\pi)^{1/3}$ (where $V_{\mathrm{b}} = 1$ μL is the bubble volume), $\eta = 10^{-3}$ Pa·s, and $\gamma = 34$ mN/m. The dashed lines represent a numerical resolution of Equation 10 (adapted in axisymmetrical geometry, with $U_{\mathrm{s}} = 0$). At the instability onset time $t_i \approx t_{\mathrm{m}}$, the minimal thickness jumps from $2h_{\mathrm{min}}(t_i)$ (*top light blue line*) to $0.7 \times 2\,h_{\mathrm{min}}(t_i)$ (*bottom light blue line*), which is the thickness of the hemi-circular patches, surrounded by a film of thickness $2h_{\mathrm{min}}(t_i)$. (*b*) Water film with interfaces covered by hexadodecanol, thin film balance. The symbols indicate experimental data from Chatzigiannakis & Vermant (2024). Solid lines are a numerical resolution of Equation 10, external conditions being given by the film size in the inset, from which the meniscus curvature and velocity are deduced (see **Figure 4**). (*c*) Solution of bovine serum albumin at 0.96 mM, rising bubble. The symbols indicate experimental data from Lin et al. (2018). Solid lines are a numerical resolution of Equation 10; dashed lines are predictions of Equation 15 with t_0 as an adjustable parameter.

Besson et al. (2008) and Bussonnière & Cantat (2021). With such setups, a direct measurement of the velocity field within the film has been performed, with either particle tracking velocimetry (Petit et al. 2015) or photobleaching techniques (Seiwert et al. 2017, Lenavetier et al. 2025).

4.3. Comparison with Experimental Data

The ability of the IIM used in Section 4.1 to predict the film behavior depends on the solution formulation and on the timescale and force scale involved. To illustrate this point, we selected a few film thickness measurements, characterized by the minimum h_{min} and maximum h_{max} of the thickness field, and compared them with the IIM predictions. In case of agreement, this identifies the nature of the flow and provides surface tension values; in case of discrepancy, it still serves as a valuable benchmark, potentially helping to identify which interface properties—such as diffusivity, viscosity, or Gibbs elasticity—govern the interface stretching.

4.3.1. Observation of an incompressible interface behavior.

The most straightforward comparisons are likely obtained for the film extraction case (see **Figure 3*e***). The good agreement between Frankel's prediction (Equation 9) and the measured thicknesses of film extracted at low Ca_{Fr} evidences an incompressible interface behavior for many surfactant solutions—though not all, as reviewed by van Nierop et al. (2008). This has mostly been studied by pulling vertical frames. However, it is also relevant in the other geometries discussed in Section 4.2, during the film expansion phase, when $\dot{R}_{\mathrm{f}} > 0$. For instance, the quasi-steady prediction from Equation 16 matches the film thickness measured by Frostad et al. (2016) at the film rim during the slow rise of a bubble toward a free surface (**Figure 5*a***).

At the end of the film formation, if the film radius stabilizes, a groove forms and deepens (Equation 15) and the tensile stress decreases (Equation 14). Thus, if the IIM holds during expansion, it should apply even better during the subsequent evolution at constant R_{f}. Yet quantitative comparisons between drainage experiments and the predictions of Equation 15 are difficult to find. One reason may be the instability of the predicted film shape—an observation illustrated in **Figure 5*a*** and discussed in Section 5. In the case of the example shown in **Figure 5*c***, the interface strongly resists shear, preventing destabilization. A comparison with the axisymmetric prediction is therefore possible and shows good agreement with Equation 15 for the groove thickness.

In highly unsteady situations—such as bubbles or droplets brought together and then separated—asymptotic regimes are never reached, and quantitative comparisons between the IIM and experiments require numerical simulations. By adapting Equation 10 to include disjoining pressure, accurate predictions have been obtained for the forces or film thicknesses in sodium dodecyl sulfate (SDS) solutions (above and below the CMC) (Dagastine et al. 2006), as well as in pure liquids (Klaseboer et al. 2000, Vakarelski et al. 2010, Lockie et al. 2011).

Similarly, the numerical solution of Equation 10 shown in **Figure 5*a*** goes beyond the quasi-steady prediction: It reproduces the transient behavior of the minimal film thickness and captures its small deviation from the IIM at larger times, which may be a signature of the finite value of the Gibbs elasticity (see **Figure 3*e***). Note that the simulation poorly reproduces the evolution of the maximal thickness, at the dimple center. The global film shape relaxes slowly by capillary leveling (see Equation 13) and is much more sensitive to the initial condition than the rim thickness. It is thus generically a less reliable indicator of interface properties than the extracted film thickness.

4.3.2. Limits of the incompressible interface model.

The meniscus exerts a tensile stress on the film of the order of $\gamma_0 H/r_\mathrm{m}$, which should be compared to $E\delta A/A$. If $H \gg h_\Gamma$, then we have $E \sim E_\mathrm{M} h_\Gamma / H$ (see Equation 7), and the condition $\delta A/A \ll 1$ becomes $\gamma_0 H^2/(r_\mathrm{m} E_\mathrm{M} h_\Gamma) \ll 1$. The IIM is therefore expected to hold more robustly at small scales.

However, the dominant factor remains the solution formulation. In pure liquids, a stress-free (extensional) regime is expected a priori. Yet even very low concentrations of surfactants can induce incompressible interface behavior. For bubbles in an SDS solution of highly controlled quality, both regimes have been observed by Liu et al. (2019), with an abrupt transition at an SDS concentration around 10 μM. Similar transitions have been indirectly observed via changes in droplet coalescence times in polymeric systems by Leal (2004) and numerically by Atasi et al. (2020). Note that in the absence of added surfactant, the agreement with IIM predictions indicates unexpected tension gradients, which are often attributed to traces of impurities. However, recent studies suggest that concentration gradients in salt solutions (Carnie et al. 2019, Liu et al. 2023, Li et al. 2025) or in liquid mixtures (Tran et al. 2022) can also induce such effects.

When molecules are absorbed at the interface, a behavior close to the IIM prediction is usually observed. A counterexample is shown in **Figure 5*b***: A water film, on which hexadodecanol has been deposited, exhibits a strong stretching behavior, leading to a fast film rupture (Chatzigiannakis & Vermant 2024), indicating, surprisingly, an almost vanishing Gibbs elasticity.

As discussed in Section 2.5, deviations from the incompressible limit may also be observed at long times. Coming back to **Figure 5*c***, a good agreement with the numerical solution of Equation 10 is found for h_min (at the rim), as well as for h_max (at the center) at short times. However, after a few seconds, h_max decreases much faster than the prediction, which may be the signature of radial surfactant diffusion, as proposed by Stebe et al. (1991) and Dai & Leal (2008) in other geometries. In that scenario, the film stretches slowly as the surfactants needed to produce interface reach the film.

Finally, some indirect influences of surfactants can further complicate the interpretation of experimental observations. Vakarelski et al. (2022) show that, in the case of buoyant bubbles reaching a free interface, changes in chemical composition alter the hydrodynamic boundary condition across the entire bubble. This affects the velocity of the bubble when it reaches the interface, thus modifying the film drainage. Similarly, out-of-equilibrium interface concentration of surfactant establishes during the bubble rise, with a depletion at the bubble front, where the film is formed (Jachimska et al. 1998, Zawala et al. 2023).

5. SYMMETRY BREAKING

5.1. Experimental Evidence of Symmetry Breaking

Most theoretical and numerical studies of film drainage assume that the system remains axisymmetric, despite clear evidence of symmetry breaking in multiple experiments. Some destabilization processes have been identified and are due to disjoining pressure (Zhang & Sharma 2018, Yilixiati et al. 2019), gravity (Lhuissier & Villermaux 2012, Shabalina et al. 2019), and evaporation (Chandran Suja et al. 2021).

However, experimental observations of axisymmetry loss during drainage have been reported in thick horizontal films (Joye et al. 1994, Velev et al. 1995, Khristov et al. 2000, Yaminsky et al. 2010, Andrieux et al. 2021), where the previous destabilizing mechanisms should be negligible.

The conditions for observing this destabilization are not entirely identified. However, it is reported by Bhamla & Fuller (2015), Frostad et al. (2016), Liu et al. (2018), and Trégouët & Cantat (2021) that the flow remains symmetric as long as the film radius increases and becomes unstable once the meniscus stops expanding. It is associated in the literature to Marangoni stress (Chatzigiannakis et al. 2021) and can be observed in systems that can be modeled by incompressible interfaces (see **Figure 5*a***). The wavelength of the instability has been measured by Trégouët & Cantat (2021) and reproduced numerically by Shi et al. (2022).

While the driving force triggering the instability has not yet been clearly determined (see Section 5.3), the primary damping mechanism is believed to be the interface shear viscosity. For a high enough resistance to shear, because of a high shear viscosity or because of a shear elastic modulus, the flow remains axisymmetrical (Lin et al. 2018).

The flow after the instability onset is better understood than the instability itself and is known as the marginal regeneration since the work by Mysels et al. (1959).

5.2. Marginal Regeneration

The loss of axisymmetry generates semicircular patches of thin film along the meniscus, separated by narrow radial channels of thicker film, connecting the central part of the film to the meniscus (see **Figure 1**). Along these channels, the velocity is directed toward the meniscus, efficiently draining the central dimple. In the thin film patches, the velocity is oriented from the meniscus toward the film (Mysels et al. 1959, Joye et al. 1994, Frostad et al. 2016, Liu et al. 2018, Gros et al. 2021).

As sketched in **Figure 6**, the fractions ξ and $1 - \xi$ of the meniscus are in contact, respectively, with film moving toward the film at a velocity v^{out} and toward the meniscus at a velocity v^{in}. This process was modeled by Mysels et al. (1959) under the following assumptions: (*a*) The interface is incompressible, enforcing the condition $\xi v^{\text{out}} = (1 - \xi) v^{\text{in}}$, and (*b*) the film and the meniscus are both at a quasi-uniform tension, respectively, $\gamma_0 + \delta\gamma$ and γ_0. Consequently, the tension difference associated with the film extracted at the velocity v^{out} (Equation 9) must balance the tension difference associated with the film entering the meniscus at v^{in}. Note that the latter is predicted by Mysels et al. (1959) but contradicts experimental observations and is corrected by an adjustable parameter in the model, as also done by Gros et al. (2021).

These constraints *a* and *b* enable prediction of the flow once the value of ξ is determined, as shown in **Figure 6*b***. In particular, they impose the thickness $2h^{\text{out}}(\xi)$ of the film extracted from the meniscus. Even though the areas of the film entering and exiting the meniscus remain equal,

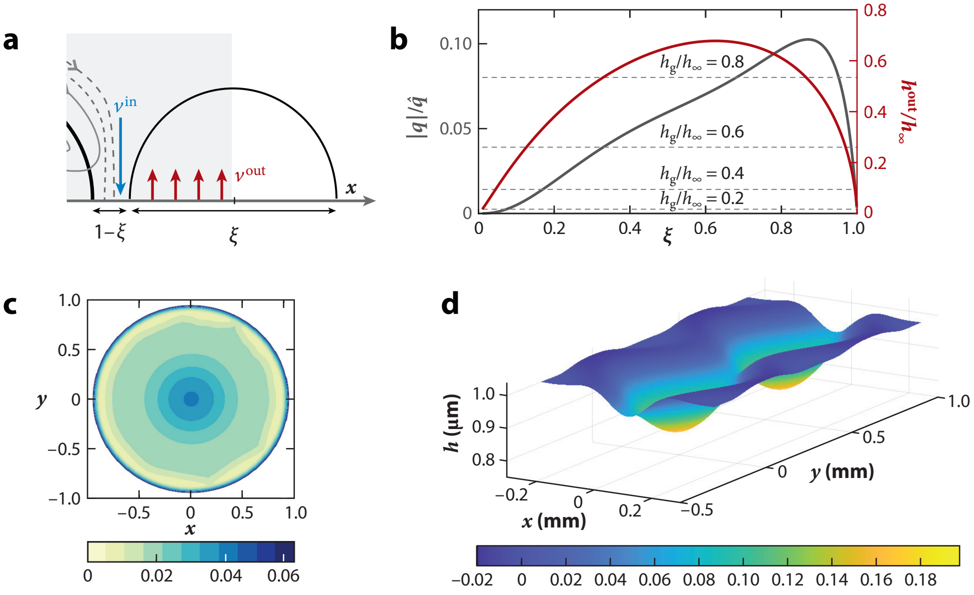

Figure 6

(*a*) Schematic of the velocity field during marginal regeneration. Panel adapted from Gros et al. (2021). (*b*) Marginal regeneration properties as a function of the ratio ξ: (*red*) film thickness in the semicircular patches relative to the thickness in the film; (*gray*) absolute value of the drainage flux either during marginal regeneration (*solid line*; Equation 17) or across the 1D groove, for different groove half-thicknesses h_g (*dashed gray lines*; Equation 14). (*c*) Thickness field. Panel adapted with permission from Shi et al. (2022). (*d*) Analytical prediction of a groove destabilization (without a meniscus). Panel adapted from Cantat & Trégouët (2025).

since $2h^{\text{out}}(\xi)$ is thinner than $2h_\infty$ for every value of ξ, the total film volume decreases over time: Marginal regeneration induces film drainage.

The value of ξ as a function of time is predicted by a kinetic model by Gros et al. (2021) for a horizontal film. However, the marginal regeneration also occurs at the bottom and on the sides of vertical films, where it was first observed. In that case, the thin film patches extracted from the bottom meniscus eventually detach due to Rayleigh–Taylor instability (Lhuissier & Villermaux 2012, Shabalina et al. 2019, Miguet et al. 2021), leaving the value of ξ in this scenario an open question. In vertical films, the patch thickness has been observed to be of the order of 0.7–0.8 h_∞ (Nierstrasz & Frens 1998). The corresponding value of ξ is slightly larger than 50% (see **Figure 6*b***).

The flux entering the half film (per unit length of meniscus), deduced by Gros et al. (2021, equations 8 and 9) is

$$q_{\text{mr}} = -\frac{\gamma_0}{\eta}\frac{h_\infty^{5/2}}{r_{\text{m}}^{3/2}}\mathcal{G}(\xi) = -\hat{q}\mathcal{G}(\xi), \qquad 17.$$

where $\mathcal{G}$ is a function of ξ shown in **Figure 6*b***.

This flux can be compared with the flux across the 1D groove. The latter is predicted by Equation 14 and can be expressed as $q_{\text{g}} = -0.14\hat{q}(h_{\text{g}}/h_\infty)^{5/2}$, so, if $(h_{\text{g}}/h_\infty)^{5/2}$ is of order one, both fluxes exhibit the same scaling. This scaling $\hat{q}$, predicted by Lhuissier & Villermaux (2012), has been experimentally observed by Vigna-Brummer et al. (2025).

For sufficiently small values of h_{g}, however, the flux induced by marginal regeneration can be much larger (in absolute value) than q_{g} (see **Figure 6*b***). The instability onset is thus associated with a strong drainage acceleration, clearly visible on the dimple height thickness measurements (see **Figure 5*a***).

5.3. Stability of 1D Solutions

The experimental observations, along with the existence of the marginal regeneration solution discussed above, clearly challenge the stability of the 1D groove built by Aradian et al. (2001) for a semiinfinite film, or by Frankel & Mysels (1962) for the dimple geometry. However, a clear description of the destabilizing process is still lacking, despite recent progress.

The instability onset is numerically reproduced in the numerical simulation of Shi et al. (2022), by solving the lubrication equations, coupled to the 3D surfactant transport, for the geometry of a bubble in contact with a free surface.

Analytically, the seminal works of Joye et al. (1994) and Bruinsma (1995) conclude that a groove in horizontal films should be stable in the limit of a large Gibbs elasticity. In both studies, linear stability analysis of the groove is performed using geometrical simplifications for the 1D flow of reference. For Joye et al. (1994), the surfactant transport, by diffusion and convection, in a film assumed locally flat, is the key process. The authors conclude that the groove is stable at a large Gibbs modulus. Bruinsma (1995) assumes the interface to be incompressible, i.e., in the large Gibbs elasticity limit, and the Poiseuille flow due to the curvature of the 1D reference shape is neglected. The conclusion is consistent with the previous study, as the groove is predicted to be stable in horizontal films.

However, experimentally, destabilization is observed for horizontal films whose behavior before or after destabilization is well-described by a model of an incompressible interface, thus in the large Gibbs elasticity limit (Gros et al. 2021) (see **Figure 5*a***).

Within this theoretical frame, an instability is evidenced by Cantat & Trégouët (2025) for a simpler geometrical case. The reference groove is based on the self-similar solution established by Benzaquen et al. (2013): Instead of being positioned between a meniscus and a flat film, it is surrounded by an infinite flat horizontal film on both sides. In this geometry, the groove is shown to be unstable in the limit of an incompressible interface if the deviatoric part of the capillary stress of the reference shape, Equation 5, which was neglected by Joye et al. (1994) and Bruinsma (1995), is taken into account. The destabilization process is purely of capillary nature and is thus reminiscent of the Rayleigh–Plateau instability (see **Figure 6*d***).

In this case of an isolated groove, the instability is due to the nonmonotonous thickness profile. Importantly, there is also a groove between the meniscus and the film, and so a nonmonotonous thickness profile, when the interface velocity is either zero (the classical dimple case) or oriented toward the meniscus (Mysels et al. 1959, Cantat 2013), two situations known to trigger the instability as discussed in Section 5.1. In contrast, the monotonic decrease in thickness observed in a film extracted at constant velocity from a meniscus, the Frankel film, always gives rise to a stable flow.

FUTURE ISSUES

1. When the incompressible interface limit is reached, soap films offer the unique opportunity to measure surface tension variations smaller than 1 mN/m through coupled hydrodynamic observations and modeling. Quantitative comparison between these inferred variations and the physicochemical properties of the solution is highly desirable. This will help address key emerging questions, such as the unexpected ability

of certain liquid phases to produce significant tension gradients or, conversely, the surprising extensibility of interfaces in systems with a seemingly high Gibbs modulus.

2. Beyond this limit, when the film interfaces are stretched, it is currently difficult to identify the respective roles of interface rheology, diffusion, and Gibbs elasticity. The development of velocity and surfactant concentration measurements would be very helpful. The latter, in particular, poses considerable experimental challenges.
3. On the theoretical side, a determination of the stability property of the groove between a film and a meniscus is needed. This would lead to deeper understanding of the marginal regeneration process and of the gravitational drainage of films. Remarkably, the beautiful circular patches of thin film rising in vertical soap films still lack theoretical predictions of their thickness.
4. Some interface shear viscosity measurements have recently been questioned, with much lower values proposed. This raises new questions about the nature of viscous damping of the fast 2D flows within foam films and the possible role of air friction.
5. Beautiful couplings have been evidenced between these complex soap film flows and other physical fields. This still offers rich perspectives for future research.

DISCLOSURE STATEMENT

The authors are not aware of any affiliations, memberships, funding, or financial holdings that might be perceived as affecting the objectivity of this review.

ACKNOWLEDGMENTS

We thank A.-L. Biance, C. Brouzet, A. Bussonnière, B. Dollet, W. Drenckhan, A. Etienne-Simonetti, T. Gaichies, T. Gauthier, T. Lenavetier, A. Monier, E. Raphaël, C. Trégouët, F. Restagno, T. Salez, J. Vermant, and A. Vigna-Brummer for their remarks and M. Chatzigiannakis and J. Frostad for sharing their data. This work was supported by Agence Nationale de la Recherche (ANR-20-CE30-0019).

LITERATURE CITED

Adelizzi EA, Troian SM. 2004. Interfacial slip in entrained soap films containing associating hydrosoluble polymer. *Langmuir* 20(18):7482–92

Andrieux S, Muller P, Kaushal M, Macias Vera NS, Bollache R, et al. 2021. Microfluidic thin film pressure balance for the study of complex thin films. *Lab Chip* 21(2):412–20

Aradian A, Raphaël E, de Gennes PG. 2001. “Marginal pinching" in soap films. *Europhys. Lett.* 55(6):834

Atasi O, Legendre D, Haut B, Zenit R, Scheid B. 2020. Lifetime of surface bubbles in surfactant solutions. *Langmuir* 36(27):7749–64

Bartlett C, Oratis AT, Santin M, Bird JC. 2023. Universal non-monotonic drainage in large bare viscous bubbles. *Nat. Commun.* 14:877

Benzaquen M, Salez T, Raphaël E. 2013. Intermediate asymptotics of the capillary-driven thin-film equation. *Eur. Phys. J. E* 36:82

Berg S, Adelizzi EA, Troian SM. 2005. Experimental study of entrainment and drainage flows in microscale soap films. *Langmuir* 21(9):3867–76

Besson S, Debrégeas G, Cohen-Addad S, Höhler R. 2008. Dissipation in a sheared foam: from bubble adhesion to foam rheology. *Phys. Rev. Lett.* 101(21):214504

Bhamla MS, Fuller GG. 2015. Placing Marangoni instabilities under arrest. *Gallery of Fluid Motion*. **https://doi.org/10.1103/APS.DFD.2015.GFM.V0040**

Biance AL, Cohen-Addad S, Höhler R. 2009. Topological transition dynamics in a strained bubble cluster. *Soft Matter* 5:4672–79

Biance AL, Delbos A, Pitois O. 2011. How topological rearrangements and liquid fraction control liquid foam stability. *Phys. Rev. Lett.* 106(6):068301

Bianco H, Marmur A. 1993. Gibbs elasticity of a soap bubble. *J. Colloid Interface Sci.* 158(2):295–302

Bird JC, de Ruiter R, Courbin L, Stone HA. 2010. Daughter bubble cascades produced by folding of ruptured thin films. *Nature* 465(7299):759–62

Breward CJW. 1999. *The mathematics of foam*. PhD Thesis, Oxford University

Breward CJW, Howell PD. 2002. The drainage of a foam lamella. *J. Fluid Mech.* 458:379–406

Bruinsma R. 1995. Theory of hydrodynamic convection in soap films. *Physica A* 216(1–2):59–76

Bussonnière A, Cantat I. 2021. Local origin of the visco-elasticity of a millimetric elementary foam. *J. Fluid Mech.* 922:A25

Cantat I. 2013. Liquid meniscus friction on a wet wall: bubbles, lamellae and foams. *Phys. Fluids* 25:031303

Cantat I, Trégouët C. 2025. Stability of an elongated thickness fluctuation in a horizontal soap film. *J. Fluid Mech.* 1003:A22

Carnie SL, Chan DYC, Lewis C, Manica R, Dagastine RR. 2005. Measurement of dynamical forces between deformable drops using the atomic force microscope. *Langmuir* 21:2912

Carnie SL, Del Castillo L, Horn RG. 2019. Mobile surface charge can immobilize the air/water interface. *Langmuir* 35(48):16043–52

Champougny L, Rio E, Restagno F, Scheid B. 2017. The break-up of free films pulled out of a pure liquid bath. *J. Fluid Mech.* 811:499–524

Champougny L, Scheid B, Restagno F, Vermant J, Rio E. 2015. Surfactant-induced rigidity of interfaces: a unified approach to free and dip-coated films. *Soft Matter* 11(14):2758–70

Chan DYC, Klaseboer E, Manica R. 2011. Film drainage and coalescence between deformable drops and bubbles. *Soft Matter* 7(6):2235–64

Chandran Suja V, Hadidi A, Kannan A, Fuller G. 2021. Axisymmetry breaking, chaos, and symmetry recovery in bubble film thickness profiles due to evaporation-induced Marangoni flows. *Phys. Fluids* 33(1):012112

Chatzigiannakis E, Jaensson N, Vermant J. 2021. Thin liquid films: where hydrodynamics, capillarity, surface stresses and intermolecular forces meet. *Curr. Opin. Colloid Interface Sci.* 53:101441

Chatzigiannakis E, Veenstra P, ten Bosch D, Vermant J. 2020. Mimicking coalescence using a pressure-controlled dynamic thin film balance. *Soft Matter* 16(41):9410–22

Chatzigiannakis E, Vermant J. 2024. Interfacial stresses in thin film drainage: subtle yet significant. *J. Rheol.* 68(4):655–63

Chesters A, Hofman G. 1982. Bubble coalescence in pure liquids. *Appl. Sci. Res.* 38:353–61

Chomaz JM. 2001. The dynamics of a viscous soap film with soluble surfactant. *J. Fluid Mech.* 442:387–409

Cohen-Addad S, di Meglio J-M. 1994. Stabilization of aqueous foam by hydrosoluble polymers. 2. Role of polymer/surfactant interactions. *Langmuir* 10(3):773–78

Couder Y, Chomaz JM, Rabaud M. 1989. On the hydrodynamics of soap films. *Physica D* 37:384–405

Dagastine RR, Manica R, Carnie SL, Chan D, Stevens GW, Grieser F. 2006. Dynamic forces between two deformable oil droplets in water. *Science* 313(5784):210–13

Dai B, Leal LG. 2008. The mechanism of surfactant effects on drop coalescence. *Phys. Fluids* 20(4):040802

Deike L. 2022. Mass transfer at the ocean–atmosphere interface: the role of wave breaking, droplets, and bubbles. *Annu. Rev. Fluid Mech.* 54:191–224

Durand M, Stone HA. 2006. Relaxation time of the topological T1 process in a two-dimensional foam. *Phys. Rev. Lett.* 97:226101

Edwards DA, Brenner H, Wasan DT. 1991. *Interfacial Transport Processes and Rheology*. Butterworth–Heinemann

Eshima J, Deike L, Stone HA. 2024. Thin-film flow due to an asymmetric distribution of surface tension and applications to surfactant deposition. *J. Fluid Mech.* 992:A2

Etienne-Simonetti A, Restagno F, Cantat I, Rio E. 2024. Hydrodynamic thinning of a coating film induced by a small solid defect: evidence of a time–minimum thickness. *Soft Matter* 20(38):7715–22

Frankel SP, Mysels KJ. 1962. On the "dimpling" during the approach of two interfaces. *J. Phys. Chem.* 66(1):190–91

Frostad JM, Tammaro D, Santollani L, Bochner de Araujo S, Fuller GG. 2016. Dynamic fluid-film interferometry as a predictor of bulk foam properties. *Soft Matter* 12(46):9266–79

Georgieva D, Cagna A, Langevin D. 2009. Link between surface elasticity and foam stability. *Soft Matter* 5(10):2063–71

Gibbs JW. 1876. *On the Equilibrium of Heterogeneous Substances*, Vol. 3. Connecticut Academy of Arts and Sciences

Gros A, Bussonnière A, Nath S, Cantat I. 2021. Marginal regeneration in a horizontal film: instability growth law in the nonlinear regime. *Phys. Rev. Fluids* 6(2):024004

Hermans E, Bhamla MS, Kao P, Fuller GG, Vermant J. 2015. Lung surfactants and different contributions to thin film stability. *Soft Matter* 11(41):8048–57

Howell PD, Stone HA. 2005. On the absence of marginal pinching in thin free films. *Eur. J. Appl. Math.* 16:569–82

Hughes B, Pailthorpe B, White L. 1981. The translational and rotational drag on a cylinder moving in a membrane. *J. Fluid Mech.* 110:349–72

Ilton M, Couchman MM, Gerbelot C, Benzaquen M, Fowler PD, et al. 2016. Capillary leveling of freestanding liquid nanofilms. *Phys. Rev. Lett.* 117(16):167801

Jachimska B, Warszynski P, Małysa K. 1998. Effect of motion on lifetime of bubbles at *n*-butanol solution surface. *Colloids Surf. A* 143(2–3):429–40

Jiang X, Rotily L, Villermaux E, Wang X. 2024. Abyss aerosols: drop production from underwater bubble collisions. *Phys. Rev. Lett.* 133(2):024001

Joly L, Detcheverry F, Biance A-L. 2014. Anomalous ζ potential in foam films. *Phys. Rev. Lett.* 113(8):088301

Joye JL, Hirasaki GJ, Miller CA. 1994. Asymmetric drainage in foam films. *Langmuir* 10(9):3174–79

Kamp J, Villwock J, Kraume M. 2017. Drop coalescence in technical liquid/liquid applications: a review on experimental techniques and modeling approaches. *Rev. Chem. Eng.* 33(1):1–47

Karakashev SI, Tsekov R, Manev ED, Nguyen AV. 2010. Elasticity of foam bubbles measured by profile analysis tensiometry. *Colloids Surf. A* 369(1–3):136–40

Kellay H. 2017. Hydrodynamics experiments with soap films and soap bubbles: a short review of recent experiments. *Phys. Fluids* 29(11):111113

Khristov K, Taylor S, Czarnecki J, Masliyah J. 2000. Thin liquid film technique—application to water–oil–water bitumen emulsion films. *Colloids Surf. A* 174(1–2):183–96

Kim I, Mandre S. 2017. Marangoni elasticity of flowing soap films. *Phys. Rev. Fluids* 2(8):082001

Klaseboer E, Chevaillier J, Gourdon C, Masbernat O. 2000. Film drainage between colliding drops at constant approach velocity: experiments and modeling. *J. Colloid Interface Sci.* 229(1):274–85

Lal J, di Meglio J-M. 1994. Formation of soap films from insoluble surfactants. *J. Colloid Interface Sci.* 164(2):506–9

Leal LG. 2004. Flow induced coalescence of drops in a viscous fluid. *Phys. Fluids* 16(6):1833–51

Lenavetier T, Audéoud G, Berry M, Gauthier A, Poryles R, et al. 2024. Line tension in a thick soap film. *Phys. Rev. Lett.* 132(5):054001

Lenavetier T, Schaub E, Cantat I. 2025. Surfactant exchanges between deformed soap films. *Phys. Rev. Lett.* 134(16):168201

Lhuissier H, Villermaux E. 2012. Bursting bubble aerosols. *J. Fluid Mech.* 696:5–44

Li D, Manica R, Chen Z, Wang S, Liu Q, Zhang H. 2025. Bubble coalescence principle in saline water. *PNAS* 122(5):e2417043122

Lian T, Matsushita S, Aoki T. 2024. A simulation study on the influence of marginal pinching upon liquid film dynamics. *Phys. Fluids* 36(11):113336

Lin CY, Slattery JC. 1982. Thinning of a liquid film as a small drop or bubble approaches a fluid–fluid interface. *AIChE J.* 28(5):786–92

Lin G, Frostad JM, Fuller GG. 2018. Influence of interfacial elasticity on liquid entrainment in thin foam films. *Phys. Rev. Fluids* 3(11):114001

Lionti-Addad S, Di Meglio JM. 1992. Stabilization of aqueous foam by hydrosoluble polymers. 1. Sodium dodecyl sulfate-poly (ethylene oxide) system. *Langmuir* 8(1):324–27

Liu B, Manica R, Liu Q, Klaseboer E, Xu Z, Xie G. 2019. Coalescence of bubbles with mobile interfaces in water. *Phys. Rev. Lett.* 122(19):194501

Liu B, Manica R, Liu Q, Xu Z, Klaseboer E, Yang Q. 2023. Nanoscale transport during liquid film thinning inhibits bubble coalescing behavior in electrolyte solutions. *Phys. Rev. Lett.* 131(10):104003

Liu B, Manica R, Zhang X, Bussonnière A, Xu Z, et al. 2018. Dynamic interaction between a millimeter-sized bubble and surface microbubbles in water. *Langmuir* 34(39):11667–75

Lockie HJ, Manica R, Stevens GW, Grieser F, Chan DY, Dagastine RR. 2011. Precision AFM measurements of dynamic interactions between deformable drops in aqueous surfactant and surfactant-free solutions. *Langmuir* 27(6):2676–85

Lucassen-Reynders E, Cagna A, Lucassen J. 2001. Gibbs elasticity, surface dilational modulus and diffusional relaxation in nonionic surfactant monolayers. *Colloids Surf. A* 186(1–2):63–72

Manikantan H, Squires TM. 2020. Surfactant dynamics: hidden variables controlling fluid flows. *J. Fluid Mech.* 892:P1

McGraw JD, Salez T, Bäumchen O, Raphaël E, Dalnoki-Veress K. 2012. Self-similarity and energy dissipation in stepped polymer films. *Phys. Rev. Lett.* 109(12):128303

Mezache Y, Detcheverry F, Di Pierro B, Spelt PDM, Biance A-L, Le Merrer M. 2024. Surfactant-induced dissipation in sheared foams: mechanics and thermodynamics. *Phys. Rev. Fluids* 9(9):094008

Miguet J, Pasquet M, Rouyer F, Fang Y, Rio E. 2021. Marginal regeneration-induced drainage of surface bubbles. *Phys. Rev. Fluids* 6(10):L101601

Mikhailovskaya A, Chatzigiannakis E, Renggli D, Vermant J, Monteux C. 2022. From individual liquid films to macroscopic foam dynamics: a comparison between polymers and a nonionic surfactant. *Langmuir* 38(35):10768–80

Modini RL, Russell LM, Deane GB, Stokes MD. 2013. Effect of soluble surfactant on bubble persistence and bubble-produced aerosol particles. *J. Geophys. Res. Atmos.* 118(3):1388–400

Motaghian M, Shirsavar R, Erfanifam M, Sabouhi M, van der Linden E, et al. 2019. Rapid spreading of a droplet on a thin soap film. *Langmuir* 35(46):14855–60

Münch A, Wagner B, Witelski TP. 2005. Lubrication models with small to large slip lengths. *J. Eng. Math.* 53:359–83

Mysels KJ, Cox MC. 1962. An experimental test of Frankel's law of film thickness. *J. Colloid Sci.* 17(2):136–45

Mysels KJ, Cox MC, Skewis JD. 1961. The measurement of film elasticity. *J. Phys. Chem.* 65(7):1107–11

Mysels KJ, Shinoda K, Frankel S. 1959. *Soap Films: Study of Their Thinning and a Bibliography*. Pergamon

Nierstrasz VA, Frens G. 1998. Marginal regeneration in thin vertical liquid films. *J. Colloid Interface Sci.* 207(2):209–17

Oron A, Davis SH, Bankoff SG. 1997. Long-scale evolution of thin liquid films. *Rev. Mod. Phys.* 69(3):931

Pasquet M, Boulogne F, Sant-Anna J, Restagno F, Rio E. 2022. The impact of physical-chemistry on film thinning in surface bubbles. *Soft Matter* 18(24):4536–42

Pasquet M, Restagno F, Cantat I, Rio E. 2023. Thickness profiles of giant soap films. *Phys. Rev. Fluids* 8(3):034001

Pereira LC, Johansson C, Blanch H, Radke C. 2001. A bike-wheel microcell for measurement of thin-film forces. *Colloids Surf. A* 186(1–2):103–11

Petit P, Seiwert J, Cantat I, Biance AL. 2015. On the generation of a foam film during a topological rearrangement. *J. Fluid Mech.* 763:286–301

Plateau JAF. 1873. *Statique expérimentale et théorique des liquides soumis aux seules forces moléculaires.* Gauthier-Villard

Poryles R, Lenavetier T, Schaub E, Bussonnière A, Saint-Jalmes A, Cantat I. 2022. Non linear elasticity of foam films made of SDS/dodecanol mixtures. *Soft Matter* 18(10):2046–53

Princen H. 1963. Shape of a fluid drop at a liquid-liquid interface. *J. Colloid Sci.* 18(2):178–95

Prins A, Arcuri C, van den Tempel M. 1967. Elasticity of thin liquid films. *J. Colloid Interface Sci.* 24(1):84–90

Prins A, van den Tempel M. 1969. Composition and elasticity of thin liquid films. *J. Phys. Chem.* 73(9):2828–34

Puthenveettil BA, Saha A, Krishnan S, Hopfinger EJ. 2018. Shape parameters of a floating bubble. *Phys. Fluids* 30(11):112105

Saint-Jalmes A, Trégouët C. 2023. Foam coarsening under a steady shear: interplay between bubble rearrangement and film thinning dynamics. *Soft Matter* 19(11):2090–98

Saulnier L, Restagno F, Delacotte J, Langevin D, Rio E. 2011. What is the mechanism of soap film entrainment? *Langmuir* 27(22):13406–9

Seiwert J, Cantat I. 2015. Generation of soap films with instantaneously adsorbed surfactants: concentration-dependent film thinning. *Colloids Surf. A* 473:2–10

Seiwert J, Dollet B, Cantat I. 2014. Theoretical study of the generation of soap films: role of interfacial visco-elasticity. *J. Fluid Mech.* 739:124–42

Seiwert J, Kervil R, Nou S, Cantat I. 2017. Velocity field in a vertical foam film. *Phys. Rev. Lett.* 118(4):048001

Seiwert J, Monloubou M, Dollet B, Cantat I. 2013. Extension of a suspended soap film: a homogeneous dilatation followed by new film extraction. *Phys. Rev. Lett.* 111:094501

Shabalina E, Bérut A, Cavelier M, Saint-Jalmes A, Cantat I. 2019. Rayleigh-Taylor-like instability in a foam film. *Phys. Rev. Fluids* 4(12):124001

Shah MS, van Steijn V, Kleijn CR, Kreutzer MT. 2019. Thermal fluctuations in capillary thinning of thin liquid films. *J. Fluid Mech.* 876:1090–107

Sheludko A. 1967. Thin liquid films. *Adv. Colloid Interface Sci.* 1(4):391–464

Shen AQ, Gleason B, McKinley GH, Stone HA. 2002. Fiber coating with surfactant solutions. *Phys. Fluids* 14:4055–68

Shi X, Fuller GG, Shaqfeh ES. 2022. Instability and symmetry breaking of surfactant films over an air bubble. *J. Fluid Mech.* 953:A26

Sonin AA, Bonfillon A, Langevin D. 1993. Role of surface elasticity in the drainage of soap films. *Phys. Rev. Lett.* 71:2342–45

Stebe KJ, Lin S-Y, Maldarelli C. 1991. Remobilizing surfactant retarded fluid particle interfaces. I. Stress-free conditions at the interfaces of micellar solutions of surfactants with fast sorption kinetics. *Phys. Fluids* 3:3–20

Stubenrauch C, von Klitzing R. 2003. Disjoining pressure isotherms of thin liquid films - new concepts and perspectives. *J. Phys. Condens. Matter* 15:R1197–232

Titta A, Le Merrer M, Detcheverry F, Spelt PDM, Biance A-L. 2018. Level-set simulations of a 2D topological rearrangement in a bubble assembly: effects of surfactant properties. *J. Fluid Mech.* 838:222–47

Toba Y. 1959. Drop production by bursting of air bubbles on the sea surface (II) theoretical study on the shape of floating bubbles. *J. Oceanogr. Soc. Jpn.* 15(3):121–30

Toshev B, Ivanov I. 1975. Thermodynamics of thin liquid films: I. Basic relations and conditions of equilibrium. *Colloid Polymer Sci.* 253:558–65

Tran HP, Passade-Boupat N, Lequeux F, Talini L. 2022. Mechanisms ruling the lifetimes of films of liquid mixtures. *J. Fluid Mech.* 944:A55

Tran T, Chakraborty P, Gioia G, Steers S, Goldburg W. 2009. Marangoni shocks in unobstructed soap-film flows. *Phys. Rev. Lett.* 103(10):104501

Trégouët C, Cantat I. 2021. Instability of the one-dimensional thickness profile at the edge of a horizontal foam film and its plateau border. *Phys. Rev. Fluids* 6(11):114005

Vakarelski IU, Manica R, Tang X, O'Shea SJ, Stevens GW, et al. 2010. Dynamic interactions between microbubbles in water. *PNAS* 107(25):11177–82

Vakarelski IU, Yang F, Thoroddsen ST. 2022. Effects of interface mobility on the dynamics of colliding bubbles. *Curr. Opin. Colloid Interface Sci.* 57:101540

van den Tempel M, Lucassen J, Lucassen-Reynders EH. 1965. Application of surface thermodynamics to Gibbs elasticity. *J. Phys. Chem.* 69:1798–804

van Nierop EA, Scheid B, Stone HA. 2008. On the thickness of soap films: an alternative to Frankel's law. *J. Fluid Mech.* 602:119–27

Velev O, Constantinides G, Avraam D, Payatakes A, Borwankar R. 1995. Investigation of thin liquid films of small diameters and high capillary pressures by a miniaturized cell. *J. Colloid Interface Sci.* 175(1):68–76

Vigna-Brummer A, Monier A, Cantat I, Brouzet C, Raufaste C. 2025. Flowing menisci: coupled dynamics and liquid exchange with soap films. *Phys. Rev. Lett.* 135:094001

Vitry Y, Dorbolo S, Vermant J, Scheid B. 2019. Controlling the lifetime of antibubbles. *Adv. Colloid Interface Sci.* 270:73–86

Yaminsky VV, Ohnishi S, Vogler EA, Horn RG. 2010. Stability of aqueous films between bubbles. Part 2. Effects of trace impurities and evaporation. *Langmuir* 26(11):8075–80

Yilixiati S, Wojcik E, Zhang Y, Sharma V. 2019. Spinodal stratification in ultrathin micellar foam films. *Mol. Syst. Des. Eng.* 4(3):626–38

Zawala J, Miguet J, Rastogi P, Atasi O, Borkowski M, et al. 2023. Coalescence of surface bubbles: the crucial role of motion-induced dynamic adsorption layer. *Adv. Colloid Interface Sci.* 317:102916

Zell ZA, Nowbahar A, Mansard V, Leal LG, Deshmukh SS, et al. 2014. Surface shear inviscidity of soluble surfactants. *PNAS* 111(10):3677–82

Zhang Y, Sharma V. 2018. Nanoridge formation and dynamics of stratification in micellar freestanding films. *Langmuir* 34(3):1208–17

Zhao Y, Xu H. 2024. Laser-induced thermocapillary flows on a flowing soap film. *Phys. Rev. Fluids* 9(2):L022001